



Non-destructive determination of the biotite crystal chemistry using Raman spectroscopy: how far we can go?

Stylianos Aspiotis¹, Jochen Schlüter², Günther J. Redhammer³, and Boriana Mihailova¹

¹Fachbereich Erdsystemwissenschaften, Universität Hamburg, Grindelallee 48, 20146 Hamburg, Germany

²Museum der Natur Hamburg – Mineralogie, Leibniz-Institut zur Analyse des Biodiversitätswandels (LIB), Grindelallee 48, 20146 Hamburg, Germany

³Fachbereich Chemie und Physik der Materialien, Paris-Lodron Universität Salzburg, 5020 Salzburg, Austria

Correspondence: Stylianos Aspiotis (stylianos.aspiotis@uni-hamburg.de)

Received: 8 July 2022 – Revised: 18 October 2022 – Accepted: 9 November 2022 – Published: 9 December 2022

Abstract. Raman spectroscopy combined with electron microprobe analysis as well as Mössbauer spectroscopy was applied to a series of 18 samples along the phlogopite ($\text{KMg}_3\text{AlSi}_3\text{O}_{10}(\text{OH})_2$)–annite ($\text{KFe}_3^{2+}\text{AlSi}_3\text{O}_{10}(\text{OH})_2$) join to establish a truly non-destructive method for crystallochemical characterization of biotite ($\text{A}_1\text{M}_3\text{T}_4\text{O}_{10}\text{X}_2$, $\text{M}_3 = \text{M1M2M2}$). The Raman scattering arising from the framework ($15\text{--}1215\text{ cm}^{-1}$) and OH-stretching phonon modes ($3000\text{--}3900\text{ cm}^{-1}$) was used to build up correlation trends between the Raman spectral features and crystal chemistry of biotite. We show that (a) the contents of $^{\text{M}}\text{Mg}$, $^{\text{M}}\text{Fe}^{2+}$, and $^{\text{M}}\text{Fe}^{3+}$ contents can be quantified with a relative error of $\sim 6\%$, $\sim 6\%$, and $\sim 8\%$, respectively, by combining the integrated intensities of the OH-stretching peaks assigned to various M1M2M2 local configurations with the wavenumber of the MO_6 vibrational mode near 190 cm^{-1} ; (b) the $^{\text{M}}\text{Ti}$ content can be estimated from the peak position and FWHM (full width at half maximum) of the second strongest TO_4 -ring mode at $\sim 680\text{ cm}^{-1}$, with a precision of 22% ; (c) the content of $^{\text{T}}\text{Si}$ can be estimated from the position of the second peak related to TO_4 -ring vibrations near 650 cm^{-1} ; (d) for phlogopite the $^{\text{T}}\text{Al}$ content can indirectly be calculated by knowing the amount of $^{\text{T}}\text{Si}$, whereas for annite it is hindered by the plausible presence of $^{\text{T}}\text{Fe}^{3+}$; (e) the $^{\text{A}}\text{K}$ content can be quantified by the position of the peak generated by T- O_b -T bond-stretching-and-bending vibration at $\sim 730\text{ cm}^{-1}$; and (f) interlayer-deficient biotites and F-rich phlogopite can be identified via their unique OH-stretching Raman peaks around 3570 cm^{-1} and 3695 cm^{-1} , respectively. Our results show a potential tool for non-destructive quantitative estimations of the major (Mg, Fe, Si, Al, K) and minor (Ti) elements of the crystal chemistry of the biotite mineral group by using a non-destructive technique such as Raman spectroscopy, although its sensitivity is generally lower than that of electron microprobe analysis and therefore cannot detect trace elements. This is fundamental within the framework of cultural heritage where samples cannot be powdered or disassembled.

1 Introduction

Phyllosilicates can be found in a variety of cultural-heritage objects such as clay tablets (e.g., Uchida et al., 2015), seals (Zazoff, 1983), earth pigments (e.g., Hradil et al., 2011; Corradini et al., 2021), blotting sand (e.g., Milke, 2012), archaeological decoration-related ceramics (e.g., Bersani and Lottici, 2016; El Halim et al., 2018), inscribed gems (e.g., Wang et al., 2013; Bersani and Lottici, 2016; Mihailova et al., 2021, and references therein), and in general as weathering prod-

ucts on the surface of common rock-forming silicate minerals (e.g., Velbel, 1993). To achieve a detailed insight into the locality and provenance of such cultural-heritage objects (e.g., Bersani and Lottici, 2016; Mihailova et al., 2021), the determination of the mineral/phase composition as well as of the crystal chemistry within each single mineral constituent is necessary.

Commonly, the crystallochemical characterization of minerals is carried out through wavelength-dispersive electron microprobe analysis (WD-EMPA) and X-ray diffrac-

tion (XRD). However, such analytical methods require special sample preparation, which is highly undesirable or even prohibitive from the viewpoint of cultural heritage, due to the uniqueness of the examined sample. X-ray fluorescence (XRF) reflection is a well-known method for non-destructive chemical characterization of samples, but the final output is just the average chemical composition of the studied object expressed in oxide weight percent (wt %), without any information about the chemistry of the individual mineral phases inside the cultural-heritage object. Besides, the detection of light element-containing mineral species, for instance H-, C-, and B-bearing, is not viable by XRF. Consequently, alternative, non-invasive, preparation-free methods such as Raman spectroscopy that can solve such challenges are becoming increasingly popular among the scientific community. The biggest advantage of Raman spectroscopy over other non-destructive analytical methods is that it can distinguish between different mineral phases within the same rock. At the same time, the exact elemental distribution within each structure type can be determined, as vibrational phonon modes are sensitive to both structure and chemistry (e.g., Bendel and Schmidt, 2008; Prencipe et al., 2012; Watenphul et al., 2016b; Waeselmann et al., 2020). Furthermore, the overall roughness of the surface does not interfere with analysis, because the use of a microscope allows for focusing down to 1–2 μm .

For a truly non-destructive crystallochemical characterization of rock-based written artifacts containing phyllosilicates, we have decided to study a series of natural biotite samples by WD-EMPA and Raman spectroscopy, because this type of layered silicates can form a complete solid solution between the magnesian endmember phlogopite ($\text{KMg}_3\text{AlSi}_3\text{O}_{10}(\text{OH})_2$) and ferrous endmember annite ($\text{KFe}_3^{2+}\text{AlSi}_3\text{O}_{10}(\text{OH})_2$) and thus can serve as model phyllosilicate group with interlayer cations.

Biotite is a trioctahedral mica with the general formula ${}^A\text{K}^M(\text{Mg}_{3-x}\text{Fe}_x^{2+})^T(\text{AlSi}_3\text{O}_{10}^X(\text{OH},\text{F})_2$, where the A site can accommodate additional minor or trace quantities of Na^+ , \square (vacancy), Ca^{2+} , and Ba^{2+} ; M refers to the octahedrally coordinated cationic site, where minor amounts of Fe^{3+} , Al^{3+} , Ti^{4+} , and Mn^{2+} and trace amounts of Cr^{3+} , Zn^{2+} , Li^+ and \square can be found; T refers to the tetrahedrally coordinated cationic site, which can also incorporate Fe^{3+} as a minor element; and X denotes the anionic site, which can be also occupied by minor or trace quantities of Cl^- and O^{2-} . Biotite crystallizes in monoclinic $C2/m$ symmetry and its structure consists of an octahedral sheet (O_s) sandwiched between two tetrahedral sheets (T_s). The T_s – O_s – T_s layers are intercalated by A-site monovalent cations (see Fig. 1), resulting in the T_s – O_s – T_s –A stacking sequence typical of biotites. Each tetrahedron shares three O atoms (bridging O atoms; O_b) with adjacent tetrahedra, thus forming a quasi-two-dimensional system of six-membered rings. The tetrahedral non-bridging O (O_{nb}) is shared with three octahedrally coordinated M cations, which are distributed between

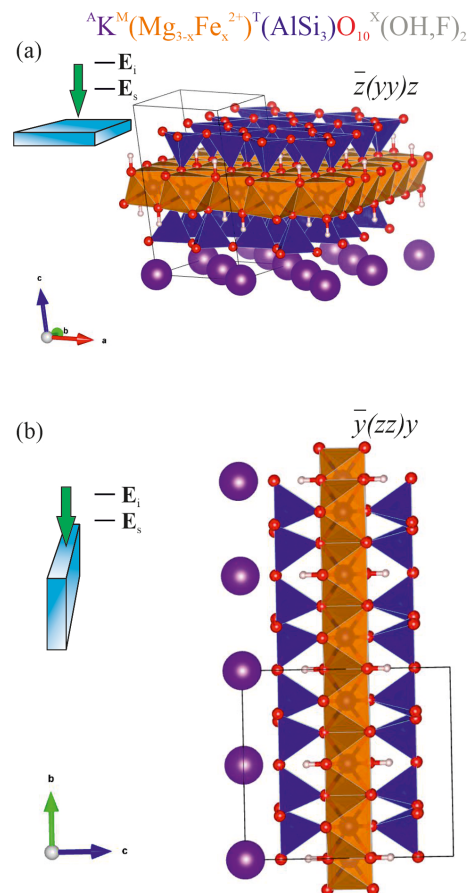


Figure 1. Sketch of the scattering geometries along with fragments of the atomic structure of biotite in the corresponding orientations: (a) horizontal orientation with the cleavage plane \perp to the laser beam direction and \parallel to E_i and (b) vertical orientation of the biotite crystal with the cleavage plane \parallel to laser beam direction and \perp to E_i . TO_4 tetrahedra are in blue; MO_6 octahedra are in orange; A-site cations are in purple; O^{2-} anions are in red; H^+ cations are in pink-whitish. VESTA software package (Momma and Izumi, 2008) was used to plot the atomic structure.

two crystallographic sites, M1 and M2, and each M1M2M2 triplet is bonded to two X-site anions. Based on single-crystal XRD analysis, it has been established that M2 is the preferred site for Ti^{4+} and Fe^{3+} , whilst divalent M cations as well as Al^{3+} are randomly partitioned on both M1 and M2 sites (e.g., Redhammer et al., 2000; Scordari et al., 2006; Lacalamita et al., 2011). Finally, A-site cations are coupled with six O_b atoms of the tetrahedral sheets.

So far, the substitutional mechanisms of biotites with various chemical compositions have been thoroughly studied by single-crystal XRD, EMPA, and Mössbauer spectroscopy (e.g., Brigatti et al., 2000; Redhammer et al., 2002; Scordari et al., 2006; Lacalamita et al., 2011; Schingaro et al., 2013). In addition, Fourier-transform infrared (FTIR) and Raman spectral features of biotites together with

peak assignment of the framework vibrational modes (15–1215 cm^{-1}) and OH-stretching modes (3550–3750 cm^{-1}) have been reported over the last 3 decades (e.g., McKown et al., 1999; Tutti and Lazor, 2008; Wang et al., 2015; Singha and Singh, 2016). Much attention has been given to the FTIR analysis of the OH-stretching peaks and their relation to different chemical configurations of M1M2M2 triplet sharing $^X(\text{OH})^-$, such as MgMgMg-OH $^-$ at 3709 cm^{-1} , MgMgFe $^{2+}$ -OH $^-$ at \sim 3695 cm^{-1} , MgMgFe $^{3+}$ -OH $^-$ near 3660–3670 cm^{-1} , MgFe $^{2+}$ Fe $^{2+}$ -OH $^-$ near 3666–3670 cm^{-1} , and Fe $^{2+}$ Fe $^{2+}$ Fe $^{2+}$ -OH $^-$ near 3640–3665 cm^{-1} (e.g., Redhammer et al., 2000; Scordari et al., 2012; Schingaro et al., 2013, and references therein). Recently, Wang et al. (2015) suggested a linear dependence of the positions of specific Raman peaks in the spectral ranges 750–780 and 3500–3800 cm^{-1} on the Fe $^{2+}$ /(Mg+Fe $^{2+}$) ratio, although they have neither separated ^TFe and ^MFe nor discriminated Fe $^{2+}$ from Fe $^{3+}$. Moreover, Tlili et al. (1989) postulated that the Raman peak of di- and trioctahedral micas at \sim 195 cm^{-1} is sensitive to ^MAl and ^TAl content, since it shifts towards higher wavenumbers with increasing both tetrahedrally and octahedrally coordinated Al content; however the number of biotite samples (a total of four) used in this study was insufficient to quantify the trend along the phlogopite–annite join.

In the present paper, we report the results of comprehensive Raman spectroscopic analyses combined with EMP and Mössbauer spectroscopy on 18 biotites with various chemical compositions, covering the whole biotite solid-solution series, aiming at establishing quantitative relationships between Raman signals (peak positions, integrated intensities, and full widths at half maximum; FWHMs) and the crystallochemical composition of the biotite-group minerals. The goals were (i) to verify whether the Raman scattering arising from the framework and OH-stretching vibrations can assist in identifying biotite-group minerals through an entirely non-destructive analytical technique; (ii) to clarify the effect of grain orientation on the Raman signals; and (iii) to understand the behavior of the major as well as minor elements (for instance Ti) within each crystallographic site as a function of the Raman signals, since they are significant crystallochemical markers that can indicate locality, a critical aspect in the field of cultural heritage.

2 Materials and methods

2.1 Samples

The biotite minerals studied here are from the mineral collection of the Mineralogical Museum, Universität Hamburg. Details about their provenance, chemical formulae, and names according to the IMA (International Mineralogical Association) nomenclature (Rieder et al., 1998) are given in Table 1.

2.2 Analytical methods

2.2.1 Wavelength-dispersive electron microprobe analysis (WD-EMPA)

EMP analyses of biotite were performed with a Cameca SX100 SEM (scanning electron microscope) system with a wavelength-dispersive detector by using the following operating conditions: 15 kV electron accelerating voltage, 20 nA beam current, and a \sim 10 μm beam-spot size on the sample surface. The employed standards were LiF for F; albite for Na; MgO for Mg; corundum for Al; andradite for Si, Ca, and Fe; vanadinite for Cl; orthoclase for K; MnTiO $_3$ for Ti and Mn; NiO for Ni; olivenite for Cu; Pb-containing glass for Zn; SrTiO $_3$ for Sr; and Ba-containing glass for Ba and Cr $_2$ O $_3$ for Cr. The acquisition times were 20 s for Mg, Al, Si, K, Ca, and Fe; 30 s for Na, Cl, and Ti; 60 s for Mn, Ni, Cu, Zn, Sr, Ba, and Cr; and 120 s for F. EMP data were acquired on 50–100 separate spots on each sample and then averaged to yield the chemical compositions and statistical standard deviations (σ) presented in Table S1 in the Supplement. The content of hydroxyl groups, as well of tetrahedrally and octahedrally coordinated Fe $^{3+}$ ($^T\text{Fe}^{3+}$ and $^M\text{Fe}^{3+}$, respectively), was calculated using the charge-balance approach of Li et al. (2020), who developed a machine learning method based on principal component regression (PCR). This method was built up on a dataset of more than 150 well-characterized biotite reference samples whose crystallochemical data have previously been refined. Biotite samples have randomly been categorized into two groups, namely the training and the test set, where the latter one has been used to testify the performance of the model and to establish a linear regression coefficient matrix. Based on the derived matrix, the atomic proportions of elements, including $^T\text{Fe}^{3+}$, $^M\text{Fe}^{2+}$, $^M\text{Fe}^{3+}$, ^XOH , and $^X\text{O}^{2-}$, can be precisely calculated with $R^2 > 0.95$ for the major elements. We have assumed that the analyzed biotite samples are lithium-free, which did not affect the quality of the calculated chemical formulae, as pointed out by Li et al. (2020). Elements whose standard deviation was greater than the average content were not included in the calculated chemical formulae. Moreover, biotite formulae were calculated by assuming that the valence state of Ti is 4+, after Scordari et al. (2013).

2.2.2 Mössbauer spectroscopy

Selected biotite samples were further subjected to ^{57}Fe Mössbauer spectroscopy to verify the fraction of Fe $^{3+}$ cations and their distribution over the T and M sites, using the setup available at the Universität Salzburg, Austria. Data were acquired at room temperature using an apparatus in a horizontal arrangement (^{57}Fe Co/Rh single-line thin source, constant acceleration mode with symmetric triangular velocity shape, multi-channel analyzer with 1024 channels, and regular velocity calibration against metallic Fe). Absorbers

Table 1. Biotite chemical formulae (in apfu, atoms per formula unit) calculated from EMPA and Mössbauer spectroscopy (for the samples with an superscripted b) on the basis of 12 anions at the X site. Sample provenance and biotite names according to IMA nomenclature (Rieder et al., 1998) are provided as well.

Sample	Location	Name	$AK^M(Mg_{3-x}Fe^{2+}_xT(AlSi_3)O_{10}^X(OH,F)_2^a$			
			Interlayer site (A)	Octahedral site (M)	Tetrahedral site (T)	Anionic site (X)
B1	York, Ontario, Canada	Sodian Fe-rich phlogopite	K _{0.84} Na _{0.12} Ba _{0.01} □ _{0.03}	Mg _{2.91} Al _{0.12} Ti _{0.07}	Si _{2.94} Al _{1.06}	OH _{1.08} F _{0.54} O _{0.38}
B2	Portland, Quebec, Canada	(OH)-rich fluorophlogopite	K _{0.92} Na _{0.02} Ba _{0.01} □ _{0.05}	Mg _{2.90} Fe _{0.07} ³⁺ Al _{0.02} Ti _{0.01}	Si _{2.97} Al _{1.03}	F _{1.10} OH _{0.84} O _{0.06}
B4 ^b	Katung River, Siberia, Russia	Tetra-ferric-containing fluorannite	K _{0.91} Na _{0.04} □ _{0.05}	Fe _{2.11} ²⁺ Fe _{0.25} ³⁺ Ti _{0.21} Mn _{0.07} Zn _{0.07} Mg _{0.05} □ _{0.23}	Si _{3.12} Al _{0.78} Fe _{0.10} ³⁺	F _{1.02} OH _{0.74} O _{0.23} Cl _{0.01}
B5	Kovdor, Russia	Octaferric phlogopite	K _{0.88} Na _{0.06} Ba _{0.02} □ _{0.04}	Mg _{2.57} Fe _{0.35} ³⁺ Ti _{0.04} Al _{0.03} □ _{0.01}	Si _{2.84} Al _{1.16}	OH _{1.67} O _{0.28} F _{0.05}
B6	Phalaborwa, South Africa	F-containing octaferric phlogopite	K _{0.89} Na _{0.03} Ba _{0.01} □ _{0.07}	Mg _{2.36} Fe _{0.30} ³⁺ Ti _{0.21} Al _{0.07} Cr _{0.01} Mn _{0.01} □ _{0.04}	Si _{2.85} Al _{1.15}	OH _{1.25} O _{0.53} F _{0.18} Cl _{0.04}
B7	Farnsen, Hamburg, Germany	(OH)-rich fluorophlogopite	K _{0.90} Na _{0.04} Ba _{0.04} □ _{0.02}	Mg _{2.85} Fe _{0.10} ³⁺ Fe _{0.01} ²⁺ Al _{0.02} Ti _{0.02}	Si _{2.86} Al _{1.14}	F _{1.21} OH _{0.77} O _{0.02}
B8	Laacher See, Eifel, Germany	Titanian ferroan oxy-rich phlogopite	K _{0.91} Na _{0.06} Ba _{0.02} □ _{0.01}	Mg _{2.12} Fe _{0.36} ³⁺ Ti _{0.31} Al _{0.19} Fe _{0.06} ³⁺ Cr _{0.01}	Si _{2.72} Al _{1.28}	OH _{1.22} O _{0.69} F _{0.09}
B10	Moravia, Romania	Octa-ferric-containing phlogopite	K _{0.91} Na _{0.03} □ _{0.06}	Mg _{2.62} Fe _{0.25} ³⁺ Al _{0.11} □ _{0.02}	Si _{2.88} Al _{1.12}	OH _{1.76} O _{0.16} F _{0.08}
B12	Upper Palatinate, Bavaria, Germany	Aluminian ferroan phlogopite	K _{0.91} Na _{0.02} □ _{0.07}	Mg _{1.18} Fe _{1.07} ²⁺ Al _{0.36} Ti _{0.16} Fe _{0.14} ³⁺ Mn _{0.02} □ _{0.07}	Si _{2.72} Al _{1.28}	OH _{1.65} O _{0.35}
B13 ^b	Johnstown, California, USA	Ti-containing magnesian annite	K _{0.89} Na _{0.02} □ _{0.09}	Fe _{1.60} ²⁺ Fe _{0.53} ³⁺ Mg _{0.39} Ti _{0.19} Al _{0.08} Mn _{0.04} □ _{0.15}	Si _{2.73} Al _{1.27}	OH _{1.60} O _{0.34} F _{0.05} Cl _{0.01}
B14 ^b	Ilimensky Mountains, Russia	Ti-containing magnesian oxy-rich annite	K _{0.94} Na _{0.05} Ba _{0.01}	Fe _{1.51} ²⁺ Mg _{0.63} Fe _{0.37} ³⁺ Ti _{0.28} Mn _{0.08} Al _{0.03} Zn _{0.01} □ _{0.07}	Si _{2.68} Al _{1.32}	OH _{1.25} O _{0.54} F _{0.21}
B16	Auvergne, France	Aluminian Fe-rich annite	K _{0.92} Na _{0.04} □ _{0.04}	Fe _{1.51} ²⁺ Al _{0.89} Mg _{0.10} Ti _{0.06} Mn _{0.06} Zn _{0.02} □ _{0.36}	Si _{2.80} Al _{1.20}	OH _{1.30} F _{0.63} O _{0.07}
B17 ^b	Sebastopol, Ontario, Canada	Ferroan (OH)-rich fluorophlogopite	K _{0.88} Na _{0.08} Ba _{0.01} □ _{0.03}	Mg _{2.01} Fe _{0.76} ²⁺ Ti _{0.12} Fe _{0.09} ³⁺ Mn _{0.02} Al _{0.01} Zn _{0.01}	Si _{2.97} Al _{1.03}	F _{0.88} OH _{0.83} O _{0.28} Cl _{0.01}
B18	Ytterby, Sweden	Magnesian interlayer-deficient annite	K _{0.63} □ _{0.37}	Fe _{1.20} ²⁺ Fe _{0.88} ³⁺ Mg _{0.70} Ti _{0.13} Al _{0.04} Mn _{0.02} □ _{0.02}	Si _{2.49} Al _{1.51}	OH _{1.66} O _{0.22} F _{0.06} Cl _{0.06}
B19 ^b	Faraday, Ontario, Canada	F-rich magnesian annite	K _{0.94} Na _{0.05} □ _{0.01}	Fe _{1.45} ²⁺ Mg _{0.86} Fe _{0.29} ³⁺ Al _{0.14} Ti _{0.09} Zn _{0.03} Mn _{0.02} □ _{0.12}	Si _{2.72} Al _{1.28}	OH _{1.42} F _{0.50} O _{0.08}
B20	Ústí nad Labem, Czech Republic	Titanian ferroan oxy-rich phlogopite	K _{0.86} Na _{0.08} Ba _{0.01} □ _{0.05}	Mg _{2.06} Fe _{0.37} ²⁺ Ti _{0.33} Al _{0.16} Fe _{0.12} ³⁺ Cr _{0.01}	Si _{2.75} Al _{1.25}	OH _{1.18} O _{0.76} F _{0.06}
B21 ^b	Kalar Mountains, Siberia, Russia	Tetra-ferric and Ti-containing fluorannite	K _{0.91} Na _{0.02} Ba _{0.01} □ _{0.05}	Fe _{2.24} ²⁺ Ti _{0.23} Fe _{0.13} ³⁺ Mn _{0.06} Zn _{0.05} Mg _{0.04} □ _{0.25}	Si _{3.22} Al _{0.67} Fe _{0.11} ³⁺	F _{1.03} OH _{0.71} O _{0.25} Cl _{0.01}

^a Cationic and anionic site occupancy is given in decreasing order of abundance.

were prepared with a nominal density of about 5 mg Fe cm^{-2} with the mica sample being filled into Cu rings, with an inner diameter of 10 mm and depth of 2 mm and fixed with epoxy resin. The spectra were recorded with the absorber being oriented at the so-called magic angle (54°) to the source to avoid texture effects. Data evaluation was done with the RECOIL program suite, using the Voigt-based hyperfine distribution approach; for details on data evaluation, see Redhammer et al. (2005).

2.2.3 Raman spectroscopy

Raman spectra were collected with a Horiba Jobin Yvon T64000 triple-monochromator system coupled with a Symphony LN₂-cooled CCD (charge-coupled device) detector and an Olympus BH41 confocal microscope with a $50\times$ long working distance objective. The green line ($\lambda = 514.532 \text{ nm}$) of a Coherent Innova 90C FreD Ar⁺ laser was used to excite the Raman scattering. The spectral resolution achieved with the green laser was $\sim 2 \text{ cm}^{-1}$, while the instrumental peak position accuracy was $\sim 0.35 \text{ cm}^{-1}$. The Raman spectrometer was calibrated using the 520.5 cm^{-1} line of a silicon standard wafer. The laser-spot diameter on the sample surface was $\sim 2 \mu\text{m}$, while the laser power on the sample surface was 7.9 mW. The spectra were collected in the spectral ranges 15–1215 and 3000–3900 cm^{-1} , with exposure times varying between 20 and 60 s and averaging 10 to 30 repeated acquisitions to improve the signal-to-noise ratio. The measured Raman spectra were baseline-corrected with a polynomial function, temperature-reduced to account for the Bose–Einstein distribution of phonons, and fitted with pseudo-Voigt peak-shape functions $PV = \mu L + (1 - \mu)G$ (L and G stand for Lorentz and Gauss peak-shape functions, respectively, while μ is a variable weight coefficient) to define the peak positions ω , FWHMs, and integrated intensities I . The usage of the OriginPro 2019 software package facilitated the Raman data evaluation.

In general, Raman peak intensities depend on the crystal orientation as well as on the mutual orientation of the polarization of the incident (E_i) and scattered light (E_s). Considering that in trioctahedral micas such as biotites the OH groups are perpendicular to the cleavage plane (Libowitzky and Beran, 2004), i.e., the crystallographic (001) plane, parallel-polarized ($E_i || E_s$) and cross-polarized ($E_i \perp E_s$) Raman spectra were collected in backscattered geometry from two different orientations of the biotite crystals, with E_i parallel (Fig. 1a) and perpendicular to the cleavage plane (Fig. 1b). This results in four scattering geometries (given in Porto's notation): horizontal parallel-polarized $\bar{z}(yy)z$, horizontal cross-polarized $\bar{z}(xy)z$, vertical parallel-polarized $\bar{y}(zz)y$, and vertical cross-polarized $\bar{y}(xz)y$ geometries, with z perpendicular to the (001) plane and $x \perp y \perp z$.

3 Results

3.1 Chemical composition from wavelength-dispersive EMPA and Mössbauer spectroscopy

The chemical composition in oxide weight percent of the studied biotites are reported in Table S1. The relatively low standard deviations reveal an overall homogenous distribution of major and minor elements among each studied biotite; i.e., the crystals are not chemically zoned. The EMPA results were initially checked for too low or too high oxide totals in weight percent, which should typically vary between 93.5 wt % and 98.5 wt %, as the H₂O content varies between 1.5 wt %–4.5 wt % (e.g., Brigatti et al., 2000, 2001; Righter et al., 2002; Laurora et al., 2007; Scordari et al., 2012; Brigatti et al., 2015). Sample B3, seemingly a tetra-ferri-containing (OH)-rich fluorophlogopite, has oxide totals_{calc} of 85.7(2.4) wt %, indicating surface defects/roughness, which in turn compromises the correct composition determined via EMPA. Therefore, the dataset of sample B3 was not taken into consideration while constructing calibration curves. On the other hand, high total oxides equal to 100 wt % can be explained by high F content such as in fluorophlogopite (e.g., Gianfagna et al., 2007; Scordari et al., 2013; Lacalamita et al., 2020). The fraction of trivalent iron and its distribution over the M and T sites for samples B4, B13, B14, B17, B19, and B21 was derived from the Mössbauer spectra (see Table S2 and Fig. S1 in the Supplement).

Following the procedures of the Excel spreadsheet by Li et al. (2020), the biotite chemical formulae were calculated in atoms per formula unit (apfu) (Table 1). As can be seen, the compositions of the studied biotites expand over the whole biotite solid-solution series with samples B1 (sodian F-rich phlogopite) and B21 (tetra-ferri- and Ti-containing fluorannite) having the highest and lowest ^MMg content, respectively.

Mineral names are given following the analytical procedures described by Rieder et al. (1998) and provided in Table 1. Sample B18 was named magnesian interlayer-deficient annite rather than interlayer-deficient mica, as the cation partitioning at the M site resembles that of a typical magnesium-rich annite (e.g., Brigatti et al., 2015), while the K content lies between 0.6 and 0.85 apfu.

3.2 Raman-scattering analysis

3.2.1 Effect of tetrahedral-octahedral layer stacking sequence in phyllosilicates

Various phyllosilicate mineral groups in a rock sample or a cultural-heritage object can straightforwardly be distinguished, based on their Raman spectra (Fig. 2). Indeed, compositional variations, the stacking sequence of the tetrahedral and octahedral sheets, and the presence or absence of interlayer species affect significantly the Raman spectra. The

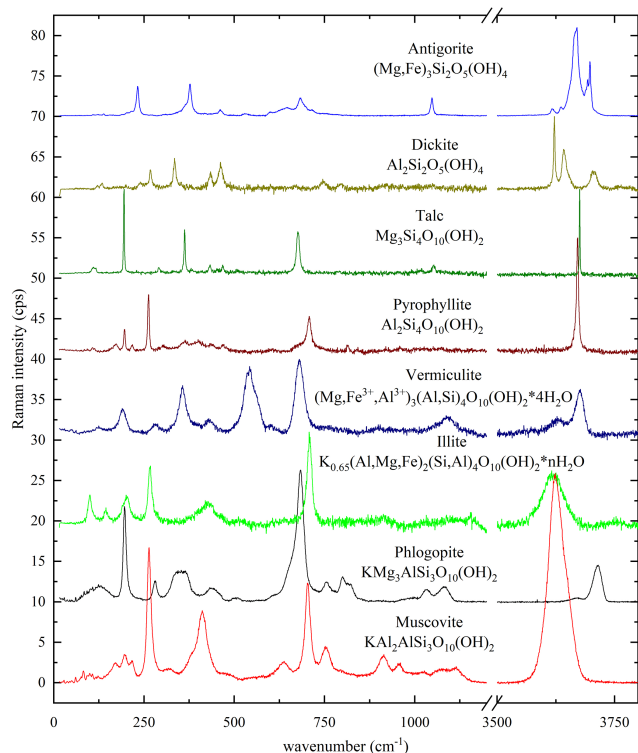


Figure 2. Raman spectra (in counts per second, cps) of various phyllosilicates. The spectra are vertically offset for clarity.

major differences in the Raman spectra of the main layered silicates (Fig. 2) are in the ranges 100–500 cm^{-1} , dominated by MO_6 vibrations; around 600–800 cm^{-1} , generated by TO_4 -ring modes (i.e., T- O_b -T modes); and 3500–3800 cm^{-1} , generated by OH-stretching vibrational modes (Tlili et al., 1989; McKeown et al., 1999; Lacalamita et al., 2020) and can be used to fingerprint the phyllosilicate mineral group. Particularly, the OH-stretching region is characterized by multiple Raman peaks in the case of 1 : 1 layer silicates (antigorite, $(\text{Mg,Fe})_3\text{Si}_2\text{O}_5(\text{OH})_4$; dickite, $\text{Al}_2\text{Si}_2\text{O}_5(\text{OH})_4$), whereas in 2 : 1 layer silicates with empty interlayer space (talc and pyrophyllite; $\text{Mg}_3\text{Si}_4\text{O}_{10}(\text{OH})_2$ and $\text{Al}_2\text{Si}_4\text{O}_{10}(\text{OH})_2$, respectively), there is only one sharp peak. If the interlayer space is filled by monovalent cations, as in the case of muscovite, biotite, or illite ($\text{K}_{0.65}(\text{Al,Mg,Fe})_2(\text{Si,Al})_4\text{O}_{10}(\text{OH})_2$), or by H_2O molecules along with mono-/divalent cations, as in the case vermiculite ($(\text{Mg,Fe}^{3+},\text{Al}^{3+})_3(\text{Al,Si})_4\text{O}_{10}(\text{OH})_2 \cdot 4\text{H}_2\text{O}$), the OH stretching produces broad Raman peaks.

3.2.2 Group-theory considerations

According to group-theory analysis, the most common $C2/m$ polytype of biotite shows a total of 63 optical phonon modes at the Γ point (Kroumova et al., 2003). Among them, 33 are IR active and 30 Raman active (see Table 2). The Raman-active modes of biotite are of A_g and B_g symmetries, and

Table 2. Group-theory analysis for the monoclinic $C2/m$ space group of biotite.

Site	Wyckoff position	Raman (A_g , B_g) and IR (A_u , B_u) active phonon modes
A_K	2b	$A_u + 2B_u$ (acoustic)
M1	2c	$A_u + 2B_u$
M2	4h	$A_g + 2B_g + A_u + 2B_u$
T	8j	$3A_g + 3B_g + 3A_u + 3B_u$
O1	8j	$3A_g + 3B_g + 3A_u + 3B_u$
O2	4i	$2A_g + B_g + 1A_u + 2B_u$
O3	8j	$3A_g + 3B_g + 3A_u + 3B_u$
X_{O4}	4i	$2A_g + B_g + 1A_u + 2B_u$
X_H	4i	$2A_g + B_g + 1A_u + 2B_u$
Total		30 Raman, 33 IR phonon modes

they have the following Raman tensor components:

$$A_g : \begin{pmatrix} a_{xx} & & a_{xz} \\ & a_{yy} & \\ a_{xz} & & a_{zz} \end{pmatrix} \text{ and } B_g : \begin{pmatrix} & a_{xy} & \\ a_{xy} & & a_{yz} \\ & a_{yz} & \end{pmatrix}.$$

Consequently, the parallel-polarized Raman spectra of oriented crystals will be generated only from the A_g modes, whereas depending on the orientation, both A_g and B_g modes can contribute to the cross-polarized spectra. In our case, the vertical parallel-polarized Raman spectra $\bar{y}(zz)y$ are determined from the zz component of the polarizability tensor α of the A_g mode, $A_g(a_{zz})$, while the vertical cross-polarized spectra $\bar{y}(xz)y$ are dominated by the $A_g(a_{xz})$. Accordingly, the horizontal parallel-polarized spectra $\bar{z}(yy)z$ are characterized by the $A_g(a_{yy})$ component, whilst the horizontal cross-polarized spectra $\bar{z}(xy)z$ are characterized by the $B_g(a_{xy})$ component. Given that the orientation of the binary b axis with respect to the laboratory coordinate axes (x, y) is usually unknown, $A_g(a_{xx})$ and $B_g(a_{zy})$ may also contribute to the horizontal parallel-polarized and vertical cross-polarized spectra, respectively.

Table 2 reveals that H atoms occupy the 4i Wyckoff position and generate $2A_g + B_g$ Raman-active modes. Considerations of the directions of the atomic vector displacements via the Bilbao Crystallographic Server (Kroumova et al., 2003) reveal that one A_g mode corresponds to the OH-stretching vibration perpendicular to the (001) plane, while one A_g and the B_g mode are related to the OH-librational modes, with H^+ motions within the (a, b) plane and causing a change in the M–O–H bond angle. Therefore, the presence of more than one Raman peaks in the OH-stretching region implies a chemical deviation from the endmember composition, due to different types of octahedrally coordinated cations bonded to OH groups. Such behavior has already been observed in other hydrous minerals like amphiboles and tourmalines (Leissner et al., 2015; Watenphul et al., 2016a; Hawthorne, 2016).

3.2.3 Effect of crystal orientation

As the structure of biotite-group minerals is strongly anisotropic, it is obvious that the Raman scattering can chiefly depend on the crystal orientation with regard to the polarization of the incident and scattered light. However, since $C2/m$ is a nonpolar crystal class, the orientation of the biotite crystals will influence the relative intensities but not the Raman peak positions. Biotite grains, which are exposed on the sample surface and can be non-destructively probed by Raman spectroscopy, can be randomly oriented. Since the relative intensities of the Raman peaks depend on the crystal orientation with respect to the polarization of the incident and scattered light, Raman spectra collected from biotite grains within the same rock/cultural-heritage specimen may appear inconsistent at a first glance. Moreover, some of the Raman peaks may be suppressed in specific experimental geometry. Therefore, to clarify the effect of the grain orientation on the Raman spectra and identify Raman signals that can be resolved independently of the grain orientation, we have systematically measured representative biotite single crystals in different scattering geometries. Figure 3 presents the Raman spectra of a phlogopite measured in the four different scattering geometries specified above. It is apparent that parallel-polarized spectra are much stronger than the cross-polarized ones, and hence the latter do not provide any additional information that is not included in the former. Therefore, A_g modes should dominate the spectra regardless of the crystal orientation. For the framework vibrations the $\bar{y}(zz)y$ spectrum differs considerably from the $\bar{z}(yy)z$, in accordance with the group-theory prediction ($a_{zz} \neq a_{yy}$). At the same time, although a_{xx} and a_{yy} are allowed to be different by symmetry constraints, in a horizontal orientation $\bar{z}(yy)z$ Raman spectra remained practically the same upon rotation of the biotite samples around the laser beam direction, indicating that the a_{xx} and a_{yy} Raman tensor components are almost equal. The OH-stretching modes contribute only to the parallel-polarized spectra, generating a multi-component Raman band. The overall OH-stretching Raman scattering is stronger in $\bar{y}(zz)y$ than in $\bar{z}(yy)z$, but the relative intensities of band components are the same in both scattering geometries. Thus, regardless of selected orientation and induced photoluminescence, the strongest Raman peaks of biotite samples can be identified at wavenumbers close to 190, 650, 680, 730, 780, and 1020 cm^{-1} and between 3500–3800 cm^{-1} and used for crystallochemical analysis.

3.2.4 Raman peak assignment and effect of chemistry

Figure 4 shows the characteristic Raman spectra of selected biotite samples with different Mg contents at the M site. One can divide the Raman scattering into four spectral ranges according to the dominant atomic displacements: range I (15–600 cm^{-1}), dominated by octahedral vibrations; range II (600–800 cm^{-1}), dominated by TO_4 -ring modes comprising

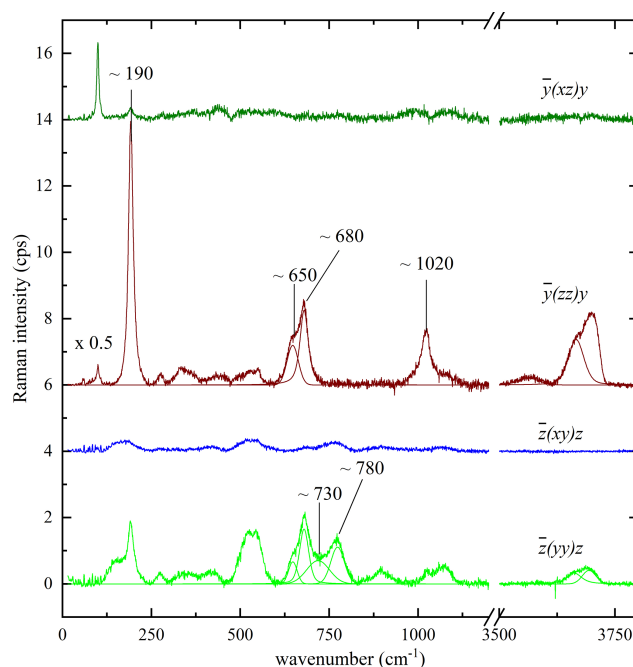


Figure 3. Raman spectra of phlogopite measured in four different scattering geometries, as described in the text. The spectra are vertically offset for clarity.

vibrations of $\text{T-O}_b\text{-T}$ linkages; range III (800–1215 cm^{-1}), generated by TO_4 -stretching modes; and range IV (3500–3800 cm^{-1}), arising from OH-stretching modes.

The strongest Raman feature of spectral range I in both parallel-polarized spectra (Fig. 4) occurs near 190 cm^{-1} for phlogopite, and it shifts considerably towards lower wavenumbers for annite with $^{\text{M}}\text{Mg} < 0.70$ apfu (Figs. 5a and 6a). As in general $\omega \sim \sqrt{\frac{K}{\mu}}$ (K is the force constant and μ is the reduced mass of atoms participating in the mode) and $m_{\text{Fe}} > m_{\text{Mg}}$ while $K(\text{Fe}^{2+}\text{-O}) > K(\text{Mg-O})$, this trend indicates one-mode behavior of the mode near 190 cm^{-1} , due to the change in mass of the M cations (Chang and Mitra, 1971). In this case, only one peak can be observed corresponding to the mixed ($\text{Mg}_{3-x}\text{Fe}_x$) concentration at the M site and whose ω lineally depends on the concentration x . Our experimental observations are in accordance with previous studies indicating that MO_6 vibrations contribute considerably to the Raman scattering below 600 cm^{-1} (Loh, 1973; Tlili et al., 1989; McKeown et al., 1999; Tutti and Lazor, 2008). Moreover, the strong Raman scattering near 150 cm^{-1} observed in monoclinic amphiboles shows the same trend of ω vs. $^{\text{M}}\text{Mg}$ content (Waeselmann et al., 2020), implying that this is a general feature of complex silicates containing strips of linked tetrahedral and octahedral sheets. Biotites are also similar to amphiboles (Waeselmann et al., 2020) by the appearance of additional Raman scattering between 500–550 cm^{-1} when $^{\text{M}}\text{Fe}^{3+}$ is present (see $\bar{z}(yy)z$ spectra in Fig. 4 and Table 1).

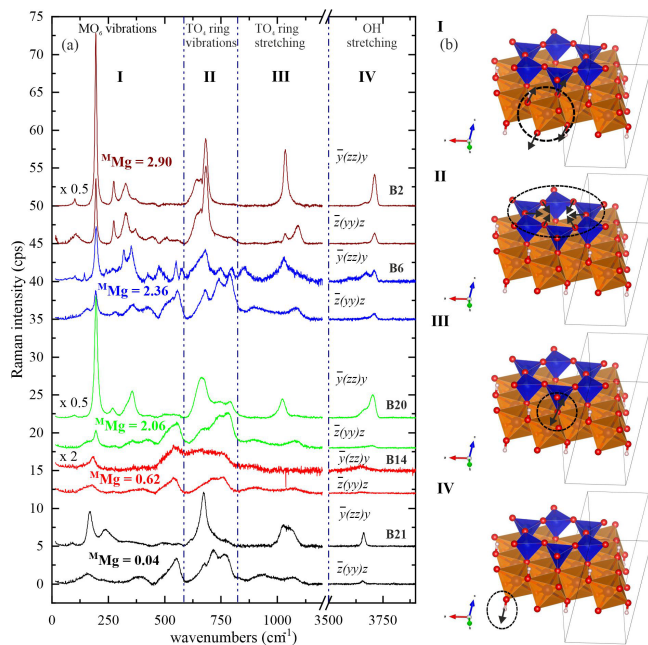


Figure 4. (a) Raman spectra of selected biotite samples with increasing octahedrally coordinated Mg content in atoms per formula unit from bottom to top. Spectra with the same color refer to the same sample and were measured in horizontal and vertical parallel-polarized geometries. The spectra are vertically offset for clarity. (b) Sketches illustrate the type of dominating atomic displacements within each spectral range (I–IV). VESTA software package (Momma and Izumi, 2008) was used to plot the atomic structures.

The spectral profile of range II changes in a rather complex way from one sample to another (Figs. 4 and S2) and can be fitted with up to four components, near 650, 680, 730, and 780 cm^{-1} . The Raman-active phonon modes near 650 and 680 cm^{-1} produce strong peaks in both $\bar{z}(yy)z$ and $\bar{y}(zz)y$ geometries, but only the wavenumber of the former mode turned to be exclusively sensitive to T-site occupancy (see Fig. 7a). In fact, this is in accordance with the peak assignment by Tlili et al. (1989) and Lacalamita et al. (2020), attributing the peaks near 650 and 680 cm^{-1} to Si–O_b–Al and Si–O_b–Si bond vibrations, respectively. Our analysis revealed that both ω_{680} and FWHM_{680} are sensitive to ^MTi content (see Fig. 7c and e). Given that Ti occupies predominantly the M2 site, this result is in agreement with previous studies suggesting that the chemistry of the M2 site can affect the T–O_b–T vibrations (e.g., McKeown et al., 1999; Wang et al., 2015; Lacalamita et al., 2020). In addition, the Raman signal near 730 cm^{-1} , well-resolved in $\bar{z}(yy)z$ and $\bar{y}(zz)y$ spectra (see Figs. 3 and 4), tends to shift to higher wavenumbers in the presence of A-site vacancies (see Fig. 8a).

We have expected the TO₄-stretching modes in range III to be sensitive to the octahedral site occupancy, as in the case of Mg–Fe–Mn amphiboles (Waeselmann et al., 2020); however, we were not able to establish a rational dependence of the

spectral parameters of these modes on the chemistry neither at the M site nor at the T site.

The reported observations for the framework phonon modes should be combined with the Raman-scattering results arising from OH-stretching modes to gain a detailed description of the entire biotite Raman spectrum and to comprehend its dependence on the site occupancy. As expected, range IV exhibits more than one peak generated by OH-stretching vibrations due to two-mode behavior, typical of complex hydrous silicates (Leissner et al., 2015; Watenphul et al., 2016a; Hawthorne, 2016). In such a case, more Raman peaks than those predicted by group-theory analysis can appear in the spectra, whose fractional intensities correlate with the composition x . This two-mode behavior of the OH-stretching phonon modes is caused by the perturbation of the $K(\text{O-H})$ force constant by the averaged M–O interactions in the surrounding triplet of MO₆ octahedra sharing oxygen atom with the X-site hydroxyl group, $\langle \delta K(\text{M-O}) \rangle$. Thus the OH-stretching wavenumber will be $\omega_{\text{OH}} \sim \sqrt{\frac{K(\text{O-H}) - \langle \delta K(\text{M-O}) \rangle}{\mu}}$, resulting in different Raman/IR peaks for different M1M2M2 chemical configurations (paper on Raman; e.g., Lacalamita et al., 2020, paper on IR; Redhammer et al., 2000). It should be emphasized that according to group theory two H⁺ in the primitive unit cell participate into the OH-stretching A_g mode. At the same time, two instances of ^X(OH)- in the chemical formula correspond to three octahedrally coordinated M cations (M1M2M2). Hence, $\langle \delta K(\text{M-O}) \rangle$ is related precisely to those three octahedra, and consequently the intensities of the OH-stretching peaks arising from different M1M2M2 triplets can be used for the correct quantification of the chemical composition of the octahedral sheets in biotite.

Table 3 presents the assignment of the multi-component Raman scattering in the OH-stretching region of the analyzed biotites to specific M-site local arrangements, following the categorization by Vedder (1964) based on the valence state of the M1M2M2 triplet surrounding the OH groups and the possibility of a vacancy at the M site: (i) the N-type bands (normal; M²⁺M²⁺M²⁺), where the hydroxyl groups are surrounded by three divalent cations; (ii) the I-type bands (impurity; M²⁺M²⁺M³⁺), where the stretching modes are caused by hydroxyl groups surrounded by one trivalent and two divalent M-site cations; and (iii) the V-type bands (vacancy; M²⁺M²⁺□/M²⁺M³⁺□/M³⁺M³⁺□), where the local atomic arrangement of the OH bonds includes a vacancy and two occupied octahedral sites.

In accordance with the two-mode behavior approach, the strongest OH-stretching peak corresponds to the most abundant M1M2M2 chemical configuration. Since biotite represents a solid solution between phlogopite and annite, where Mg and Fe²⁺ are the dominant octahedrally coordinated cations, for each biotite sample the most intense OH-stretching peak should correspond to the most probable M²⁺M²⁺M²⁺ chemical species. Hence, weaker

Table 3. Raman peak assignment of the OH-stretching vibrations associated with various local configurations of the octahedrally coordinated cations.

Horizontal				Vertical			
Sample	Wavenumber	Local configuration	Reference	Sample	Wavenumber	Local configuration	Reference
B1, B2, B5, B6, B7, B8, B10, B17, B20	3705–3716	MgMgMg-OH ⁻ -K-OH ⁻	Thili et al. (1989), Scordari et al. (2006), Lacalamita et al. (2011, 2020)	B1, B2, B5, B6, B7, B10, B17, B20	3708–3714	MgMgMg-OH ⁻ -K-OH ⁻	Thili et al. (1989), Scordari et al. (2006), Lacalamita et al. (2011, 2020)
B3	3696	MgMgMg-OH ⁻ -K-F ⁻	This work	B3	3696	MgMgMg-OH ⁻ -K-F ⁻	This work
B8, B12, B17, B20	3692–3698	MgMgFe ²⁺ -OH ⁻ -K-OH ⁻	Lacalamita et al. (2011), Scordari et al. (2012)	B8, B10, B12, B17, B20	3693–3701	MgMgFe ²⁺ -OH ⁻ -K-OH ⁻	Lacalamita et al. (2011), Scordari et al. (2012)
B6, B8, B10, B20	3681–3686	MgMgMg-OH ⁻ -K-O ²⁻	Scordari et al. (2006, 2012)	B5, B8, B10, B20	3681–3686	MgMgMg-OH ⁻ -K-O ²⁻	Scordari et al. (2006, 2012)
B12, B13, B14, B18, B19	3671–3676	MgFe ²⁺ Fe ²⁺ -OH ⁻	Lacalamita et al. (2011)	B12, B13, B14, B19	3674–3677	MgFe ²⁺ Fe ²⁺ -OH ⁻	Lacalamita et al. (2011)
B1, B2, B3, B5, B6, B7, B10, B17, B20	3660–3670	MgMgFe ³⁺ -OH ⁻ -K-OH ⁻ or MgMgAl-OH ⁻ -K-OH ⁻	Thili et al. (1989), Scordari et al. (2006, 2012), Lacalamita et al. (2011), Schingaro et al. (2013)	B1, B2, B3, B5, B6, B7, B10, B17, B20	3660–3672	MgMgFe ³⁺ -OH ⁻ -K-OH ⁻ or MgMgAl-OH ⁻ -K-OH ⁻	Thili et al. (1989), Scordari et al. (2006, 2012), Lacalamita et al. (2011), Schingaro et al. (2013)
B4, B12, B13, B14, B16, B18, B19, B21	3648–3656	Fe ²⁺ Fe ²⁺ Fe ²⁺ -OH ⁻ -K-OH ⁻	Redhammer et al. (2000)	B4, B12, B13, B14, B16, B18, B19, B21	3647–3660	Fe ²⁺ Fe ²⁺ Fe ²⁺ -OH ⁻ -K-OH ⁻	Redhammer et al. (2000)
B12	3625–3630	Fe ²⁺ Fe ²⁺ Fe ³⁺ -OH ⁻ -K-OH ⁻ or AlAl□-OH ⁻ -K-OH ⁻	Redhammer et al. (2000), Libowitzky and Beran (2004), Scordari et al. (2008)	B4, B12, B13, B14, B18, B19	3625–3630	Fe ²⁺ Fe ²⁺ Fe ³⁺ -OH ⁻ -K-OH ⁻ or AlAl□-OH ⁻ -K-OH ⁻	Redhammer et al. (2000), Libowitzky and Beran (2004), Scordari et al. (2008)
B12, B18, B19	3600–3607	MgMg□-OH ⁻	Kodama et al. (1974), Lacalamita et al. (2020)	B6, B12, B14, B16	3600–3603	MgMg□-OH ⁻	Kodama et al. (1974), Lacalamita et al. (2020)
B16	3596	Fe ²⁺ Al□-OH ⁻ -K-OH ⁻	Redhammer et al. (2000)				
B18	3570	Fe ²⁺ Fe ²⁺ Fe ³⁺ -OH ⁻ -Al□-OH ⁻	This work	B18	3570	Fe ²⁺ Fe ²⁺ Fe ³⁺ -OH ⁻ -Al□-OH ⁻	This work

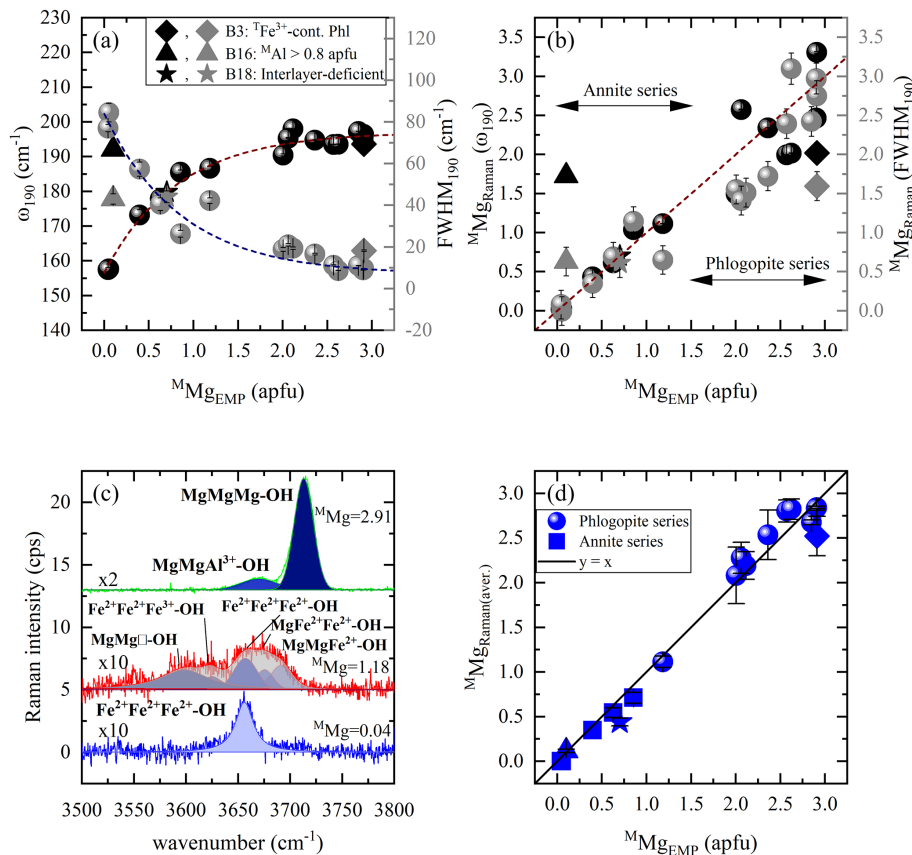


Figure 5. Estimation of Mg content according to MO_6 vibrations and OH-stretching peaks: (a) Raman peak position at $\sim 190\text{ cm}^{-1}$ vs. Mg (black symbols) and $FWHM_{190}$ vs. Mg (gray symbols), (b) Mg content derived from the Raman spectroscopic analysis (Mg_{Raman}) of ω_{190} (black symbols) and $FWHM_{190}$ (gray symbols) vs. that calculated from EMPA (Mg_{EMP}), and (c) OH-stretching vibrations of three representative biotites (Mg-richest, sample B1; Mg-poorest, sample B21; with an intermediate composition, sample B12) are presented in horizontal parallel-polarized spectra. (d) Mg_{EMP} vs. Mg_{Raman} of the OH-stretching region of both parallel-polarized geometries. Deviating points in panels (a), (b), and (d): rhombus for a Fe^{3+} -containing OH-rich phlogopite (Phl), triangle for an aluminian F-rich annite with $MAl > 0.8$ apfu, and star for a magnesian interlayer-deficient annite.

OH-stretching peaks will correspond to less probable M1M2M2 local configurations. Consequently, peaks related to MgMgMg-OH⁻-K-X local configurations are observed for all of the studied phlogopite samples (B1, B2, B3, B5, B6, B7, B8, B10, B17, and B20) with the exception of sample B12, which shows an intermediate composition in the octahedral layer (see Table 1). However, the peak position slightly varies depending on the X-site anion adjacent to ^AK. Furthermore, the majority of the phlogopite samples exhibits OH-stretching modes in the range $3660\text{--}3670\text{ cm}^{-1}$ corresponding to MgMgFe³⁺ and MgMgAl, whose OH groups are involved in an OH⁻-K-OH⁻ local environment (Tlili et al., 1989; Scordari et al., 2006; Lacalamita et al., 2011; Scordari et al., 2012; Schingaro et al., 2013). It is worth noting that the gradual substitution of Mg by Al at the M site, emerging from the Al-Tschermak substitution mechanism, will downshift the peak position of the initial MgMgMg-OH⁻-K-OH⁻ local configuration by $\sim 30\text{--}35\text{ cm}^{-1}$, i.e., from $\sim 3705\text{--}3715$ to $3670\text{--}3675\text{ cm}^{-1}$. This assumption corroborates the conclu-

sions by Hawthorne et al. (2000), Scordari et al. (2012), and Watenphul et al. (2016a), who showed that a similar Raman peak shift towards lower frequencies has been monitored for the OH-stretching peaks in tremolites and phlogopite as well as for the W-site OH stretching in tourmalines.

At the same time, most of the examined annite samples (B4, B13, B14, B16, B18, B19, and B21) display the strongest OH-stretching N-type Raman peak between 3650 and 3660 cm^{-1} (Figs. S2 and S3, Table 3), corresponding to Fe²⁺Fe²⁺Fe²⁺-OH⁻-K-X (Redhammer et al., 2000). For sample B16, an aluminian F-rich annite, the Raman peak at $\sim 3596\text{ cm}^{-1}$ is assigned to a Fe²⁺Al□-OH⁻ local configuration (Redhammer et al., 2000) rather than to MgMg□-OH⁻, by taking into account the following aspects: (i) the peak centered at $\sim 3596\text{ cm}^{-1}$ being the strongest feature of the $\bar{z}(yy)z$ Raman spectrum of sample B16 (Fig. S2), indicating that it should be assigned to the most abundant cations at the M site, and (ii) the cationic distribution of the M site with $MFe^{2+} = 1.54$ apfu, $MAl = 0.88$ apfu, and $MMg = 0.10$ apfu.

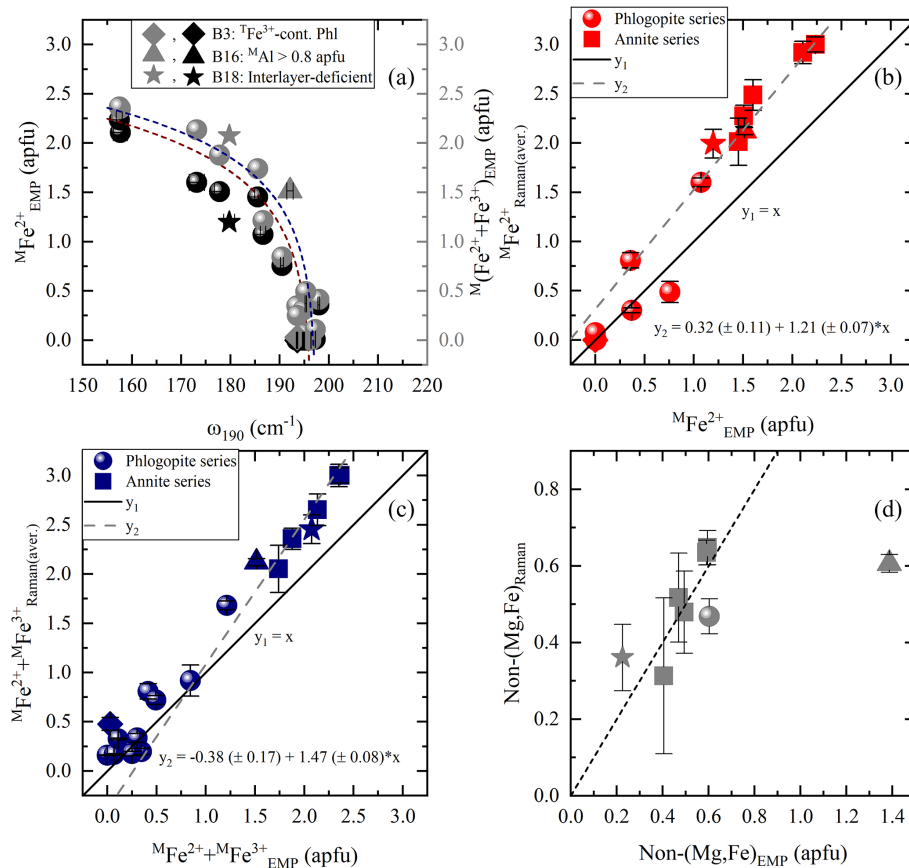


Figure 6. Estimation of $M_{\text{Fe}^{2+}}$ and $M_{\text{Fe}^{2+} + \text{Fe}^{3+}}$ contents according to MO_6 vibrations and OH-stretching peaks: (a) $M_{\text{Fe}^{2+}}$ amount vs. Raman peak position at 190 cm^{-1} (black symbols) and $M_{\text{Fe}^{2+} + \text{Fe}^{3+}}$ content vs. ω_{190} (gray symbols), (b) $M_{\text{Fe}^{2+}}$ from the Raman spectroscopic analysis ($M_{\text{Fe}^{2+}}^{\text{Raman}}$) of the OH-stretching vibrations vs. that calculated from EMPA ($M_{\text{Fe}^{2+}}^{\text{EMP}}$), and (c) $M_{\text{Fe}^{2+} + \text{Fe}^{3+}}$ from the Raman spectroscopic analysis ($M_{\text{Fe}^{2+} + \text{Fe}^{3+}}^{\text{Raman}}$) of the OH-stretching region vs. that calculated from EMPA ($M_{\text{Fe}^{2+} + \text{Fe}^{3+}}^{\text{EMP}}$). (d) Non-(Mg,Fe) cationic content at the M site of the samples deviating from the one-to-one correlation lines of Fig. 6b and c, where the non-(Mg,Fe) amount from the Raman spectroscopic analysis ($\text{non}-(\text{Mg,Fe})_{\text{Raman}}$) was plotted vs. that calculated from EMPA ($\text{non}-(\text{Mg,Fe})_{\text{EMP}}$). Deviating data points mentioned in the legend are same as in Fig. 5.

4 Discussion

4.1 Major elements in the octahedral sheets

Quantification of M_{Mg} content in atoms per formula unit can be achieved by the Raman signals of two different vibrational groups (Fig. 5). The best candidate from the framework vibrational modes are the MO_6 vibrations at $\sim 190 \text{ cm}^{-1}$, whose peak position and FWHM are plotted against M-site Mg concentration (Fig. 5a). Data points of both plots were fitted with the exponential functions $\omega_{190} = (197.1 \pm 0.3) - 40.57e^{-1.213M_{\text{Mg}}}$ and $\text{FWHM}_{190} = (6.8 \pm 2.6) + (77.1 \pm 16.8)e^{(-1.2 \pm 0.3)M_{\text{Mg}}}$, respectively. Then, using the inverse functions $M_{\text{Mg}}(\omega_{190}) = \frac{\ln 40.57 - \ln[197.1 - \omega_{190}]}{1.213}$ and $M_{\text{Mg}}(\text{FWHM}_{190}) = \frac{\ln 77.1 + \ln[\text{FWHM}_{190} - 6.8]}{1.2}$, one can calculate the content of M_{Mg} from the Raman data ($M_{\text{Mg}}^{\text{Raman}}$). It is worth noting that sample B16, an aluminian F-rich annite, strongly

deviates from both exponential trends in Fig. 5a, which we attribute to the high amount of octahedrally coordinated Al > 0.8 apfu, the highest among the studied biotites; consequently an alternative should be found to quantify M_{Mg} in such M_{Al} -rich biotites. Moreover, $M_{\text{Mg}}^{\text{Raman}}$ plotted against $M_{\text{Mg}}^{\text{EMP}}$ (Fig. 5b) reveals relatively large deviation from the one-to-one correlation line for phlogopite ($M_{\text{Mg}} > 1.5$ apfu). Hence, the introduction of a second vibrational group sensitive to M-site occupancy by Mg is mandatory to solve this issue.

As pointed out above, the M-site chemistry has a strong effect on the OH-stretching modes, in a way very similar to that for amphiboles (Leissner et al., 2015; paper on IR; e.g., Hawthorne, 2016). The correct assignment of the OH-stretching peaks to different chemical M1M2M2 species is however, a key factor for the proper utilization of the two-mode behavior approach, since the peak position of the strongest OH-stretching Raman peak will reveal

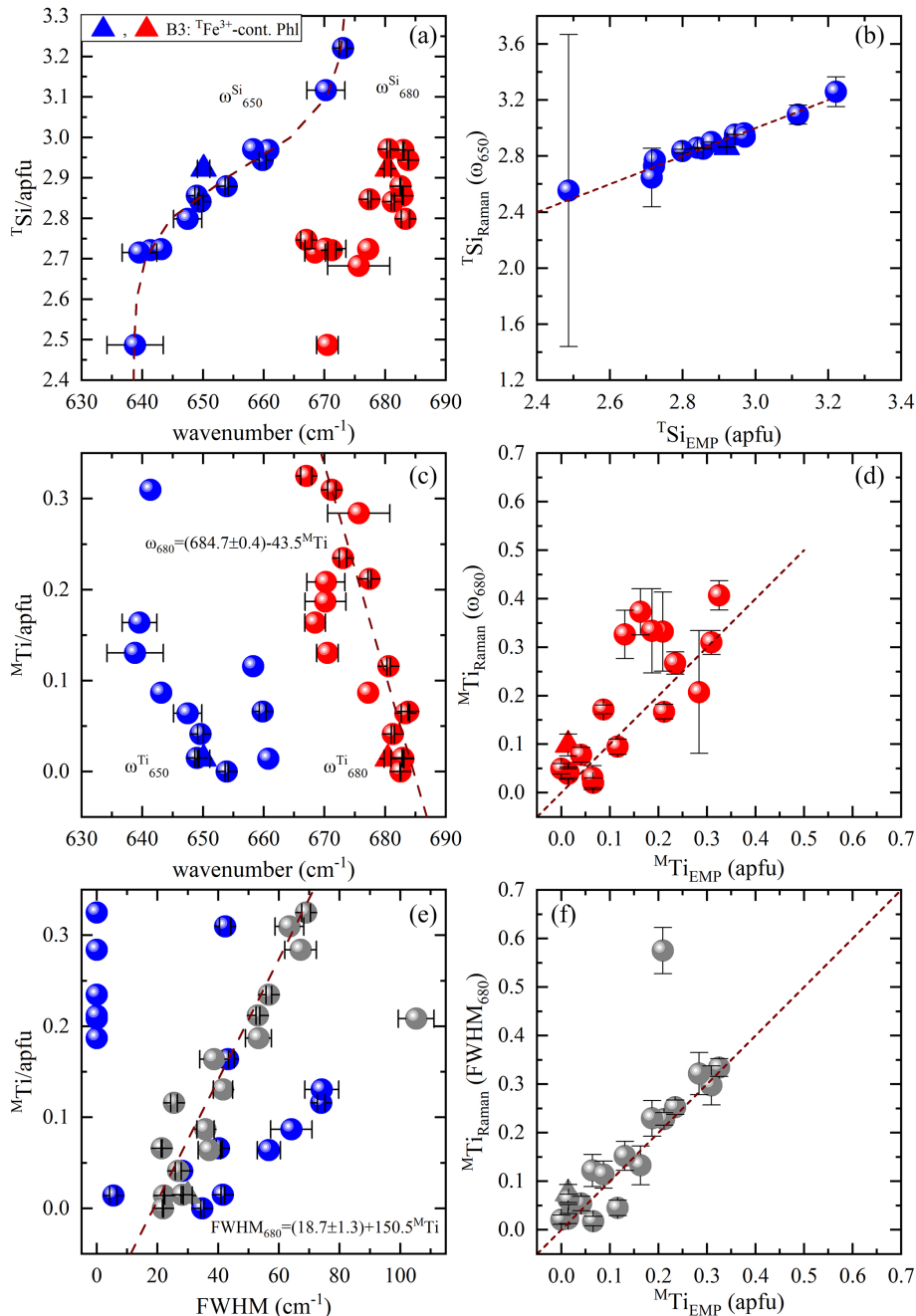


Figure 7. Estimation of ^TSi and ^MTi contents in accordance with the TO_4 -ring modes near 650 and 680 cm^{-1} : (a) ^TSi amount vs. Raman peak position at ~ 650 (blue symbols) and $\sim 680 \text{ cm}^{-1}$ (red symbols), (b) ^TSi content derived from the Raman spectroscopic analysis ($^T\text{Si}_{\text{Raman}}$) of ω_{650} vs. that determined from EMPA ($^T\text{Si}_{\text{EMP}}$), (c) ^MTi content vs. Raman peak position at ~ 650 (blue symbols) and $\sim 680 \text{ cm}^{-1}$ (red symbols), (d) ^MTi content obtained from the Raman spectroscopic analysis ($^M\text{Ti}_{\text{Raman}}$) of ω_{680} vs. that determined from EMPA ($^M\text{Ti}_{\text{EMP}}$), (e) ^MTi amount vs. FWHM at ~ 650 (blue symbols) and $\sim 680 \text{ cm}^{-1}$ (gray symbols), and (f) ^MTi content obtained from the Raman spectroscopic analysis ($^M\text{Ti}_{\text{Raman}}$) of FWHM_{680} vs. that determined from EMPA ($^M\text{Ti}_{\text{EMP}}$).

the dominant cations occupying the octahedral layer. We have attributed the observed OH-stretching peaks based on multiple studies by others (see Table 3, Fig. 5c). Then the content of ^MMg was calculated by averaging the sum of the integrated I of each parallel-polarized orientation

($\bar{z}(yy)z$ and $\bar{y}(zz)y$) generated by Mg-containing M1M2M2 configurations, multiplied by the number of Mg cations in the corresponding triplet: $^M\text{Mg}_{\text{Raman}}(\text{horizontal}),(\text{vertical}) =$

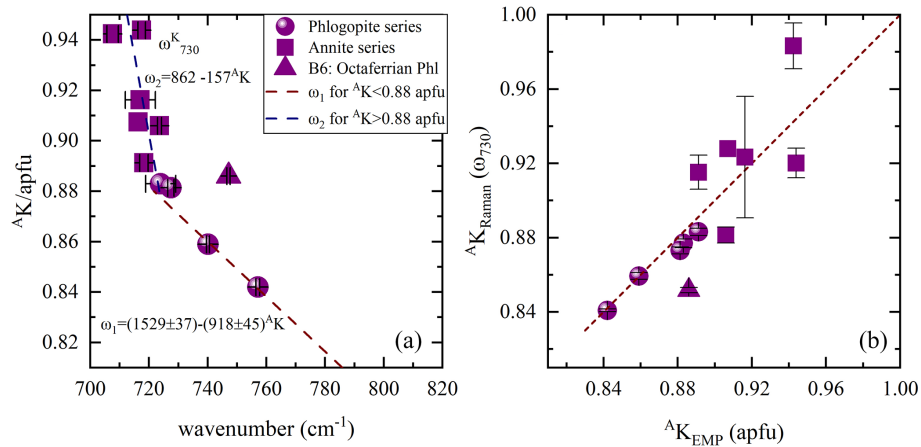


Figure 8. (a) Content of A-site coordinated K vs. ω_{730} , where the Raman spectroscopic data are emerging from the $\bar{y}(zz)y$ scattering geometry, while in (b) ${}^A K_{\text{Raman}}$ vs. ${}^A K_{\text{EMP}}$ estimated from both ω_1 and ω_2 linear trends in (a). Deviating point: triangle indicates sample B6, a phlogopite containing octahedrally coordinated Fe^{3+} at concentrations of ~ 0.30 apfu.

$$\frac{3I_{\text{MgMgMg-OH-K-OH}} + 3I_{\text{MgMgMg-OH-K-F}} + 2I_{\text{MgMgFe}^{2+}} + 3I_{\text{MgMgMg-OH-K-O}^{2-}} + I_{\text{MgFe}^{2+}\text{Fe}^{2+}} + 2I_{\text{MgMgFe}^{3+}} + 2I_{\text{MgMgAl}} + 2I_{\text{MgMg}\square}}{I_{\text{OH (total)}}},$$

where $I_{\text{OH(total)}}$ the sum of the integrated intensities of all OH-stretching modes in both $\bar{z}(yy)z$ and $\bar{y}(zz)y$ Raman spectra; in the case of a single-crystal grain with unknown orientation or polycrystalline sample, $I_{\text{OH(total)}}$ can be simply the intensity summed up over all OH-stretching Raman peaks. The ${}^M\text{Mg}_{\text{Raman (aver.)}}$ values plotted against those calculated from the EMP analysis (${}^M\text{Mg}_{\text{EMP}}$) exhibit an excellent one-to-one correlation (Fig. 5d).

It is worth commenting more in detail on the OH-stretching peak assignment of B18 (magnesian ${}^A\text{K}$ -deficient annite). The Raman peak at 3570 cm^{-1} observed in the spectrum of B18 was assigned to $\text{Fe}^{2+}\text{Fe}^{2+}\text{Fe}^{3+}\text{-OH}^- \text{-A}\square\text{-OH}^-$ rather than to $\text{Fe}^{3+}\text{Al}\square\text{-OH}^- \text{-K-OH}^-$, which generates an infrared absorption peak in close proximity in energy (Redhammer et al., 2000), based on the following decisive criteria: (i) this is the strongest Raman signal in the OH-stretching range, and therefore it can be hardly attributed to defects in the octahedral layer. (ii) B18 is the only interlayer-deficient biotite among all the samples studied here, with a considerable amount of A-site vacancies (${}^A\text{K}_{0.63}\square_{0.37}$). (iii) B18 is ${}^M\text{Al}$ -poor annite; i.e., Fe^{2+} and Fe^{3+} are the most abundant octahedrally coordinated cations. (iv) Previous Raman and infrared studies on amphiboles (Leissner et al., 2015; Hawthorne, 2016) indicated that an OH-stretching peak generated by a given triplet of MO_6 octahedra next to A-site vacancy is downshifted in wavenumber by approximately $50\text{--}60\text{ cm}^{-1}$ with respect to the OH-stretching peak generated by the same MO_6 triplet but next to a filled A-site, which favors a $\text{Fe}^{2+}\text{Fe}^{2+}\text{Fe}^{3+}$ over a $\text{Fe}^{2+}\text{Fe}^{2+}\text{Fe}^{2+}$ configuration (compare the corresponding peak positions related to ${}^A\text{K}$ in Table 3). It should be men-

tioned that a perfect match of sample B18 with the one-to-one line of Fig. 5d can be achieved by taking into consideration the influence of ${}^T\text{Al}$ on the ω of the M1M2M2 triplets in the $\bar{z}(yy)z$ scattering geometry, since B18 has the highest content of tetrahedrally coordinated Al in the sample suite studied here (${}^T\text{Al} = 1.51$ apfu). Previous research on the ${}^T\text{Al}$ effect in synthetic amphiboles with vacant A sites (Hawthorne et al., 2000) and along the annite–siderophyllite ($\text{K}(\text{Fe}_2^+, \text{Al})(\text{Si}_2\text{Al}_2)\text{O}_{10}(\text{OH})_2$) join with fully occupied A sites (Redhammer et al., 2000) indicated that progressive substitution of ${}^T\text{Si}$ by ${}^T\text{Al}$ resulted in a downshift of the OH-stretching bands by $15\text{--}20\text{ cm}^{-1}$. This accounts principally for the N- and I-type OH Raman peaks in the case of ${}^T\text{Al}$ -rich annite. Thus, the peaks at 3677 and 3655 cm^{-1} of the horizontal parallel-polarized spectrum of B18 should rather be assigned to $\text{MgMgFe}^{2+}\text{-OH}^-$ and $\text{MgFe}^{2+}\text{Fe}^{2+}\text{-OH}^-$ local arrangements, respectively. Therefore, an ${}^M\text{Mg}_{\text{Raman (aver.)}}$ value of 0.73 apfu can be obtained, which is almost identical to 0.70 apfu of the EMP analysis. Nevertheless, the cross-checking of the calculations gained from Fig. 5b and d will reduce the uncertainties and give an unequivocal determination of ${}^M\text{Mg}$ content of sample B18.

Nominally biotite is an ${}^M(\text{Mg}, \text{Fe}^{2+})$ solid solution, and therefore ω_{190} as a function of the ${}^M\text{Fe}^{2+}$ content shows a reverse trend (see Fig. 6a) compared to that against ${}^M\text{Mg}$ content (Fig. 5a). Consequently, ${}^M\text{Fe}^{2+}$ content can be estimated using the equation $\omega_{190} = (196.6 \pm 0.3) - 0.891e^{(1.71 \pm 0.20)M\text{Fe}^{2+}}$. However, similarly to the case of ${}^M\text{Mg}$ (Fig. 5b), there is an unsatisfactory deviation of the phlogopite dataset from the one-to-one-correlation (see Fig. S4). Since the ${}^M\text{Mg}$ content could be quantified more precisely by the integrated I of OH-stretching modes, the same strategy was followed to quantify ${}^M\text{Fe}^{2+}$, using the equation ${}^M\text{Fe}^{2+}_{\text{Raman (horizontal), (vertical)}} =$

$$\frac{I_{\text{MgMgFe}^{2+}} + 2I_{\text{MgFe}^{2+}\text{Fe}^{2+}} + 3I_{\text{Fe}^{2+}\text{Fe}^{2+}\text{Fe}^{2+}} + 2I_{\text{Fe}^{2+}\text{Fe}^{2+}\text{Fe}^{3+}} + I_{\text{Fe}^{2+}\text{Al}\square}}{I_{\text{OH (total)}}},$$

where $I_{\text{OH (total)}}$ the sum of the integrated intensities of all OH-stretching modes of the horizontal and vertical parallel-polarized spectra, respectively. Figure 6b shows the correlation of ${}^{\text{M}}\text{Fe}_{\text{Raman (aver.)}}^{2+}$ with ${}^{\text{M}}\text{Fe}^{2+}$ concentration determined by EMPA, where the data points for Mg-rich biotites with ${}^{\text{M}}\text{Fe}^{2+} < 0.8$ apfu follow a one-to-one correlation line and for Fe-rich biotites (with ${}^{\text{M}}\text{Fe}^{2+} > 0.8$ apfu) a linear trend that can be expressed by the relation ${}^{\text{M}}\text{Fe}_{\text{Raman (aver.)}}^{2+} = (0.32 \pm 0.11) + (1.21 \pm 0.07) \cdot {}^{\text{M}}\text{Fe}_{\text{EMP}}^{2+}$.

It should be underlined that the presence of ${}^{\text{M}}\text{Fe}^{3+}$ also affects the peak position of the MO_6 vibrations at $\sim 190 \text{ cm}^{-1}$, which increases exponentially with increasing ${}^{\text{M}}(\text{Fe}^{2+} + \text{Fe}^{3+})$ content and can be calculated by $\omega_{190} = 197.5 - (0.67 \pm 0.27)e^{(1.76 \pm 0.25)({}^{\text{M}}(\text{Fe}^{2+} + \text{Fe}^{3+}))}$ (Fig. 6a). Besides that, the integrated intensities of the OH-stretching modes, where Fe^{3+} is involved in the assigned local environment and is mainly emerging from the MgMgFe^{3+} and $\text{Fe}^{2+}\text{Fe}^{2+}\text{Fe}^{3+}$ triplets for phlogopite and annite, respectively, can be used to quantify the total amount of octahedrally coordinated Fe and then plotted against ${}^{\text{M}}(\text{Fe}^{2+} + \text{Fe}^{3+})_{\text{EMP}}$ (Fig. 6c). Similarly to the trends in Fig. 6b, good one-to-one correlation can be achieved for phlogopite with ${}^{\text{M}}(\text{Fe}^{2+} + \text{Fe}^{3+}) < 0.8$ apfu, whilst for samples exceeding this value, ${}^{\text{M}}(\text{Fe}^{2+} + \text{Fe}^{3+})$ content can be obtained from ${}^{\text{M}}(\text{Fe}^{2+} + \text{Fe}^{3+})_{\text{Raman (aver.)}} = (-0.38 \pm 0.17) + (1.47 \pm 0.08) \cdot {}^{\text{M}}(\text{Fe}^{2+} + \text{Fe}^{3+})_{\text{EMP}}$.

The fact that ${}^{\text{M}}\text{Fe}^{2+}$ and ${}^{\text{M}}(\text{Fe}^{2+} + \text{Fe}^{3+})$ are overestimated by Raman spectroscopy, while ${}^{\text{M}}\text{Mg}$ is not, suggests that additional non-magnesium, non-iron elements contribute to the spectral range dominated by OH-stretching modes related to ferrous/ferric M1M2M2 configurations. This is also evident by the overall broad bands (FWHM $\sim 27\text{--}40 \text{ cm}^{-1}$) in the range $3650\text{--}3660 \text{ cm}^{-1}$ in the $\bar{z}(yy)z$ Raman spectra of annite samples (B13, B14, B16, B18, and B19), indicating a superposition of multiple different octahedrally coordinated cationic combinations such as $\text{Fe}^{2+}\text{Fe}^{2+}\text{Fe}^{3+}$, $\text{Fe}^{2+}\text{Fe}^{2+}\text{Al}$, and $\text{AlAl}\square$ (e.g., Redhammer et al., 2000; Libowitzky and Beran, 2004; Scordari et al., 2008; Schingaro et al., 2013). Hence, subtle amounts of minor elements such as Al, Ti, and Mn, entering the M site, whose vibrational modes cannot be separated from the ascribed ones, lead to the deviation of the annite dataset from the one-to-one correlation lines of Fig. 6b and c. This can be seen by plotting the contents of the non-(Mg,Fe) octahedrally coordinated cations calculated from the Raman and EMP analyses (Fig. 6d), where a one-to-one match with discrepancies within the relative errors is observed for all samples. The only exception is sample B16, characterized by an unusual high content of non-(Mg,Fe) cations of almost 47% of the M-site occupancy. By subtracting the excess of ${}^{\text{M}}\text{Fe}^{2+}$ ($y_2(x)$ in Fig. 6b) from the total amount of octahedrally coordinated ($y_2(x)$ in Fig. 6c), one can estimate ${}^{\text{M}}\text{Fe}_{\text{Raman (aver.)}}^{3+} = (-0.70 \pm 0.20) + (0.26 \pm 0.11) \cdot {}^{\text{M}}\text{Fe}_{\text{EMP}}^{3+}$, which is signifi-

cant in Earth sciences, as it is indicative of oxidation processes. We could not find a satisfactory trend to directly quantify ${}^{\text{M}}\text{Fe}^{3+}$, e.g., via ω and integrated I of the Raman scattering in the range $500\text{--}550 \text{ cm}^{-1}$, which is noticeable spectral indicators for the presence of octahedrally coordinated Fe^{3+} in Na amphiboles (Waeselmann et al., 2020).

4.2 Major elements in the tetrahedral sheets

Among the framework phonon modes the TO_4 -ring modes near 650 and 680 cm^{-1} (i.e., T–O_b–T bending) appear to be most sensitive to the T-site occupancy (see Fig. 7a). However, the position of the Raman peak near 680 cm^{-1} (Si–O_b–Si) turned to be also sensitive to the content of ${}^{\text{T}}\text{Ti}$ (see the discussion below), whereas the position of the peak near 650 cm^{-1} (Si–O_b–Al) is indifferent to the M-site occupancy. Therefore, we propose to use the wavenumber of the TO_4 -ring mode near 650 cm^{-1} to estimate the amount of ${}^{\text{T}}\text{Si}$. The evolution of ω_{650} with respect to ${}^{\text{T}}\text{Si}$ can be fitted with a Boltzmann-type function $\omega_{650} = 673.5 + (638.5\text{--}673.5)/(1 + e^{\frac{{}^{\text{T}}\text{Si}-2.92}{0.078}})$, and then the ${}^{\text{T}}\text{Si}$ amount can be quantified by the inverse function ${}^{\text{T}}\text{Si} = 0.078 \cdot [\ln(\omega_{650} - 638.5) - \ln(673.5 - \omega_{650})] + 2.92$ (see Fig. 7a). Only sample B3 slightly deviates from fitting trend, an effect that can be connected to the incorporation of Fe^{3+} at the T site. Despite that, the plot of ${}^{\text{T}}\text{Si}$ amount derived from the Raman data against ${}^{\text{T}}\text{Si}_{\text{EMP}}$ provides an excellent one-to-one correlation for all values between 2.6 and 3.2 apfu with a relative uncertainty of $\sim 3\%$ (Fig. 7b). Due to the sigmoidal shape of the ${}^{\text{T}}\text{Si}(\omega_{650})$ curve, the uncertainty in determining ${}^{\text{T}}\text{Si}$ considerably increases for values below 2.6 apfu.

The common tetrahedrally coordinated elements in biotite are Si, Al, and trivalent Fe, but ${}^{\text{T}}\text{Fe}^{3+}$ is usually found in annite rather than in phlogopite. Therefore, for phlogopite the amount of tetrahedrally coordinated Al cations can be also determined: ω_{650} as ${}^{\text{T}}\text{Al} = 4 - {}^{\text{T}}\text{Si}(\omega_{650})$ apfu. This can help in general to cross-check the correctness of OH-stretching assignment, which is significant for the refinement of the M-site occupancy, because studies on the annite-siderophyllite ($\text{K}(\text{Fe}_2^+, \text{Al})(\text{Si}_2\text{Al}_2)\text{O}_{10}(\text{OH})_2$) join (Redhammer et al., 2000) as well as on amphiboles with vacant A sites (Hawthorne et al., 2000) revealed that the progressive substitution of ${}^{\text{T}}\text{Al}$ for ${}^{\text{T}}\text{Si}$ results in a downshift of the OH-stretching mode by $15\text{--}20 \text{ cm}^{-1}$.

4.3 Presence of M-site Ti

Interestingly, the position and FWHM of the TO_4 -ring mode at $\sim 680 \text{ cm}^{-1}$, involving Si–O_b–Si-bond-bending vibrations exhibit a linear correlation with the ${}^{\text{M}}\text{Ti}$ (Fig. 7c and e, respectively), without showing any dependence on the major M-site elements. This is probably related to the fact that tetravalent Ti interacts stronger with the TO_4 apical oxygen atoms, resulting in subtle change of the TO_4 -ring tilt geometry and thus influencing the T–O–T-bending vi-

brations. The linear fits to the corresponding data points yielded $\omega_{680} = (684.7 \pm 0.4) - 43.5^{\text{M}\text{Ti}}$ and $\text{FWHM}_{680} = (18.7 \pm 1.3) + 150.5^{\text{M}\text{Ti}}$. As can be seen in Fig. 7d and f several data points for annite (samples B4, B12, B13, and B18) derived from $^{\text{M}\text{Ti}}(\omega_{680})$ deviate from the one-to-one trend, whereas the dispersion is considerably less for the data derived from $^{\text{M}\text{Ti}}(\text{FWHM}_{680})$. Thus, using the relation $^{\text{M}\text{Ti}} = [\text{FWHM}_{680} - (18.7 \pm 1.3)]/150.5$, one can determine $^{\text{M}\text{Ti}}$ with a relative uncertainty of $\sim 20\%$. The only deviating point in the trend showed in Fig. 7f is sample B4, in whose spectrum the two peaks near 650 and 680 cm^{-1} could not be resolved and appeared as a single very broad Raman peak centered at $\sim 670 \text{ cm}^{-1}$ with $\text{FWHM}_{680} = 105.3 \text{ cm}^{-1}$ (Fig. 7e). It should be mentioned that in Ti-rich biotites ($^{\text{M}\text{Ti}} > 0.2$ apfu) contributions from OH stretching of X-site hydroxyl groups shared between Ti-containing M1M2M2 triplets can be expected (e.g., Scordari et al., 2006). However, to keep local charge balance, commonly the anionic X sites next to $^{\text{M}\text{Ti}}$ are occupied by an O^{2-} -forming local chemical arrangement of type $\text{K-O}^{2-}\text{-M}^{2+}\text{M}^{2+}\text{Ti}^{4+}\text{-O}^{2-}\text{-K}$, in which no OH-stretching peaks should be observed. Possible Raman-active modes of the OH-stretching vibrations, including Ti in the assigned triplets to comply with the requirements for local charge balance can be $\text{K-OH}^{-}\text{-M}^{2+}\text{Ti}^{4+}\text{-OH}^{-}\text{-K}$, $\text{K-O}^{2-}\text{-M}^{2+}\text{M}^{2+}\text{Ti}^{4+}\text{-OH}^{-}\text{-A}$ or less probably $\text{A-O}^{2-}\text{-M}^{2+}\text{M}^{2+}\text{Ti}^{4+}\text{-OH}^{-}\text{-K}$. Such considerations are supported by the main substitution mechanisms involving Ti after Li et al. (2020). However, we could not resolve such additional OH-stretching peaks in our Ti-rich samples, namely phlogopite B6, B8, and B20 and annite B4, B14, and B21.

4.4 Interlayer cations

In contrast to earlier findings by Wang et al. (2015), a direct connection of the linearly increasing $\text{Fe}^{2+}/(\text{Mg} + \text{Fe}^{2+})$ ratio with decreasing ω of the Raman peaks at 715–755 (ω_{730}) and 760–780 cm^{-1} (ω_{780}) could not be observed. Though, the peak position of the ring mode vibrations at $\sim 730 \text{ cm}^{-1}$ in the $\bar{y}(zz)y$ Raman spectra tends to be sensitive to the occupancy of the interlayer space and shifts linearly to higher wavenumbers in the presence of A-site vacancies with a gradient change at $^{\text{M}\text{Mg}}$ contents of 1.5 apfu. This tendency reflects to some extent the evolution of $^{\text{A}\text{K}}$ content with increasing ω_{730} values. Accordingly, $^{\text{A}\text{K}}$ content was only plotted against ω_{730} (Fig. 8a), as ω_{780} could not mirror the amount of A-site cations, in particular of K. For biotites belonging to the phlogopite series $^{\text{A}\text{K}}$ content can be determined by using the equation $\omega_1 = (1529 \pm 37) - (918 \pm 45)^{\text{A}\text{K}}$, while that of annite can be expressed by the relation $\omega_2 = 862 - 157^{\text{A}\text{K}}$. The Raman-scattering analysis provides precise calculation of the amount of $^{\text{A}\text{K}}$ for the phlogopite dataset with a relative error of $\sim 3\%$, but the uncertainty obtained from the inverse trend of ω_1 is too large to quantify $^{\text{A}\text{K}}$ content of annite (Fig. 8b). Sample B6 deviates

from the ω_2 linear trend and is characterized by $^{\text{M}\text{Fe}^{3+}}$ contents of ~ 0.30 apfu. Though, it cannot be stated whether the elevated $^{\text{M}\text{Fe}^{3+}}$ contents in the crystal structure of phlogopite shift the corresponding peak towards higher wavenumbers, since in sample B5, an octaferrian phlogopite with similar amount of $^{\text{M}\text{Fe}^{3+}}$, we could not identify a peak between 715 and 755 cm^{-1} .

4.5 Limitations of the method

Raman spectroscopy, as with any other analytical technique, has its limitations, and undoubtedly, it cannot achieve the detection limit of EMPA ($\sim 100\text{--}200$ ppm), and trace elements cannot be detected by Raman spectroscopy. Besides, the uncertainties in the quantification of major and minor elements by Raman spectroscopy are affected by the quality of the measured spectra, i.e., by the signal-to-noise ratio and spectral resolution. Nevertheless, here we demonstrate that the relative uncertainties of $^{\text{T}\text{Si}}$, $^{\text{A}\text{K}}$, $^{\text{M}\text{Mg}}$, $^{\text{M}\text{Fe}^{2+}}$, and $^{\text{M}\text{Fe}^{3+}}$ amounts in atoms per formula unit, as derived from Raman-scattering data, are 3 %, 3 %, 6 %, 6 %, and 8 %, respectively, whereas the uncertainties in the chemical formulae calculated from EMP data are $\sim 1\%$ – 2% . Moreover, the determination of Fe^{3+} only on the basis of EMPA is not straightforward. Minor elements such as $^{\text{M}\text{Ti}}$ can be estimated by Raman spectroscopy with a relatively large uncertainty of 20 % against 6 % by EMPA.

5 Conclusions

The results of our combined Raman spectroscopic and WD-EMPA as well as Mössbauer analyses clearly reveal that the major cations occupying the octahedral, tetrahedral, and interlayer sites of biotites can be determined with acceptable relative errors. Minor elements at the M site such as Ti, which are critical crystallochemical markers indicative of specimen locality, can be quantified as well. According to the overall spectral profile, one can easily distinguish between phlogopite and annite, as the strongest MO_6 peak (region I; Fig. 4) appears at ~ 195 and 165 cm^{-1} , respectively, while the strongest OH-stretching peak (region IV; Fig. 4) is at 3710 and 3650 cm^{-1} , respectively. Furthermore, the established calibration curves between the Raman signals and the chemical composition of the analyzed biotites provide a preparation-free, fast, and easy-to-handle tool for the crystallochemical characterization of those phyllosilicates. Guidelines for non-specialists to non-destructively determine the crystallochemical composition of biotites are listed as follows:

1. By following the recommended OH-stretching peak assignment to different local cationic arrangements (Table 3), $^{\text{M}\text{Mg}}_{\text{Raman (aver.)}}$, $^{\text{M}\text{Fe}^{2+}}_{\text{Raman (aver.)}}$, and $^{\text{M}(\text{Fe}^{2+} + \text{Fe}^{3+})}_{\text{Raman (aver.)}}$ can be calculated.

- Deviations from the one-to-one correlation lines, in the case of estimating the ${}^M\text{Fe}^{2+}$ and ${}^M\text{Fe}^{3+}$ amounts, demonstrate incorporation of non-(Mg,Fe) cations in the octahedral layer (Fig. 6d).
- The amount of M-site Mg, Fe^{2+} , and Fe^{3+} can be cross-checked by the position of the strong Raman peak near 190 cm^{-1} , arising from the MO_6 vibrations; in the case of ${}^M\text{Mg}$, FWHM_{190} can be used as well.
- ${}^M\text{Ti}$ content can be quantified by the peak position and FWHM of the TO_4 -ring mode at $\sim 680\text{ cm}^{-1}$. Due to smaller relative errors, it is recommended to use the ${}^M\text{Ti}(\text{FWHM}_{680})$ trend if two peaks near 650 and 680 cm^{-1} can be resolved.
- The presence of ${}^M\text{Al} > 0.8$ apfu in annite can be detected by cross-checking the ${}^M\text{Mg}$ contents derived from ω_{190} and of the integrated intensities of the OH-stretching peaks.
- The amount of ${}^T\text{Si}$ can be monitored using the peak position of the TO_4 -ring modes at $\sim 650\text{ cm}^{-1}$. ${}^T\text{Al}$ content of phlogopite can indirectly be extracted by ${}^T\text{Al} = 4 - {}^T\text{Si}$.
- Potassium deficiency in phlogopite larger than 0.12 apfu can be quantified from the position of the peak at $\sim 730\text{ cm}^{-1}$. Interlayer-deficient annite can be recognized by the position of the strongest OH-stretching mode, appearing at 3570 instead of $\sim 3650\text{ cm}^{-1}$.

Overall, our study shows that Raman spectroscopy is a reliable experimental method for the crystallochemical characterization also for biotites along with other complex hydrous silicates, though still not so precise as EMPA. However, the truly non-destructive nature of Raman spectroscopy makes it an extremely useful tool for characterizing cultural-heritage objects, and the trends provided here demonstrate that it can be used even for quantitative analyses. Moreover, one can directly analyze mineral grains in thin sections as prepared for polarization microscopy. It is highly anticipated that a similar analytical approach to other groups of phyllosilicates, including those that can be found in cultural-heritage artifacts, could facilitate the non-invasive determination of their crystallochemical composition.

Data availability. Data derived from this research are presented in the Supplement. Additional data are available upon request from the corresponding author.

Supplement. The supplement related to this article is available online at: <https://doi.org/10.5194/ejm-34-573-2022-supplement>.

Author contributions. BM and JS initiated the project. SA carried out the Raman experiments as well as the Raman and EMP data evaluation and analyses. GJR performed the Mössbauer spectroscopic analysis. SA prepared the manuscript with contributions from BM and JS. All authors discussed and interpreted the results.

Competing interests. The contact author has declared that none of the authors has any competing interests.

Disclaimer. Publisher's note: Copernicus Publications remains neutral with regard to jurisdictional claims in published maps and institutional affiliations.

Acknowledgements. The research for this study was funded by the Deutsche Forschungsgemeinschaft (DFG, German Research Foundation) under Germany's Excellence Strategy for "Understanding Written Artefacts: Material, Interaction and Transmission in Manuscript Cultures" (EXC 2176; project no. 390893796). The research was conducted within the scope of the Centre for the Study of Manuscript Cultures (CSMC) at Universität Hamburg. We thank Stefanie Heidrich and Peter Stutz, Universität Hamburg, for helping with WD-EMPA measurements and sample preparation. We are very grateful to the Mineralogical Museum of Universität Hamburg for kindly providing the whole of the biotite crystals.

Financial support. This research has been supported by the Deutsche Forschungsgemeinschaft (grant no. EXC 2176 "Understanding Written Artefacts: Material, Interaction and Transmission in Manuscript Cultures").

Review statement. This paper was edited by Tiziana Boffa Ballaran and reviewed by Monika Koch-Müller and one anonymous referee.

References

- Bendel, V. and Schmidt, B. C.: Raman spectroscopic characterization of disordered alkali feldspars along the join $\text{KAlSi}_3\text{O}_8\text{-NaAlSi}_3\text{O}_8$: application to natural sanidine and anorthoclase, *Eur. J. Mineral.*, 20, 1055–1065, <https://doi.org/10.1127/0935-1221/2009/0021-1856>, 2008.
- Bersani, D. and Lottici, P. P.: Raman spectroscopy of minerals and mineral pigments in archaeometry, *J. Raman Spectrosc.*, 47, 499–530, 2016.
- Brigatti, M. F., Frigieri, P., Ghezzi, C., and Poppi, L.: Crystal chemistry of Al-rich biotites coexisting with muscovites in peraluminous granites, *Am. Mineral.*, 85, 436–448, 2000.
- Brigatti, M. F., Kile, D. E., and Poppi, M.: Crystal structure and crystal chemistry of Lithium-bearing muscovite-2 M_1 , *Can. Mineral.*, 39, 1171–1180, 2001.
- Brigatti, M. F., Affronte, M., Elmi, C., Malferrari, D., and Laurora, A.: Trioctahedral Fe-rich micas: Relationships between magnetic

- behavior and crystal chemistry, *Am. Mineral.*, 100, 2231–2241, 2015.
- Chang, I. F. and Mitra, S. S.: Long wavelength optical phonons in mixed crystals, *Adv. Phys.*, 20, 359–404, 1971.
- Corradini, M., de Ferri, L., and Pojana, G.: Spectroscopic characterization of commercial pigments for pictorial retouching, *J. Raman Spectrosc.*, 52, 35–58, 2021.
- El Halim, M., Daoudi, L., El Ouahabi, M., Rousseau, V., Cools, C., and Fagel, N.: Mineralogical and geochemical characterization of archaeological ceramics from the 16th century El Badi Palace, Morocco, *Clay Miner.*, 53, 459–470, 2018.
- Gianfagna, A., Scordari, F., Mazziotti-Tagliani, S., Ventruti, G., and Ottolini, L.: Fluorophlogopite from Biancavilla (Mt. Etna, Sicily, Italy): Crystal structure and crystal chemistry of a new F-dominant analog of phlogopite, *Am. Mineral.*, 92, 1601–1609, 2007.
- Hawthorne, F. C.: Short-range atomic arrangements in minerals. I: The minerals of the amphibole, tourmaline and pyroxene supergroups, *Eur. J. Mineral.*, 28, 513–536, <https://doi.org/10.1127/ejm/2016/0028-2538>, 2016.
- Hawthorne, F. C., Welch, M. D., Della Ventura, G., Liu, S., Robert, J.-L., and Jenkins, D. M.: Short-range order in synthetic aluminous tremolites. An infrared and triple-quantum MAS NMR study, *Am. Mineral.*, 85, 1716–1724, 2000.
- Hradil, D., Pířková, A., Hradilová, J., Bezdička, P., Lehrberger, G., and Gerzer, S.: Mineralogy of Bohemian green earth pigment and its microanalytical evidence in historical paintings, *Archaeometry*, 53, 563–586, 2011.
- Kodama, H., Ross, G. J., Iiyama, J. T., and Robert, J.-L.: Effect of layer charge location on potassium exchange and hydration of micas, *Am. Mineral.*, 59, 491–495, 1974.
- Kroumova, E., Aroyo, M. I., Perez-Mato, J. M., Kirov, A., Capillas, C., Ivantchev, S., and Wondratschek, H.: Bilbao Crystallographic Server: useful databases and tools for phase-transition studies, *Phase Transit.*, 76, 155–170, 2003.
- Lacalamita, M., Schingaro, E., Scordari, F., Ventruti, G., Fabbrizio, A., and Pedrazzi, G.: Substitution mechanisms and implications for the estimate of water fugacity for Ti-rich phlogopite from Mt. Vulture, Potenza, Italy, *Am. Mineral.*, 96, 1381–1391, 2011.
- Lacalamita, M., Schingaro, E., Mesto, E., Zaccarini, F., and Biagioni, C.: Crystal-chemistry of micas belonging to the yangzhumingite-fluorophlogopite and phlogopite-fluorophlogopite series from the Apuan Alps (northern Tuscany, Italy), *Phys. Chem. Miner.*, 47, 54, <https://doi.org/10.1007/s00269-020-01118-2>, 2020.
- Laurora, A., Brigatti, M. F., Mottana, A., Malferrari, D., and Caprilli, E.: Crystal chemistry of trioctahedral micas in alkaline and subalkaline rocks: A case study from Mt. Sassetto (Tolfa district, Latium, central Italy), *Am. Mineral.*, 92, 468–480, 2007.
- Leissner, L., Schlüter, J., Horn, I., and Mihailova, B.: Exploring the potential of Raman spectroscopy for crystallochemical analyses of complex hydrous silicates: I. Amphiboles, *Am. Mineral.*, 100, 2682–2694, 2015.
- Li, X., Zhang, C., Behrens, H., and Holtz, F.: Calculating biotite formula from electron microprobe analysis data using a machine learning method based on principal components regression, *Lithos* 356–357, 105371, <https://doi.org/10.1016/j.lithos.2020.105371>, 2020.
- Libowitzky, E. and Beran, A.: IR spectroscopic characterization of hydrous species in minerals, in: *Spectroscopic methods in mineralogy*, edited by: Beran, A. and Libowitzky, E., EMU Notes in Mineralogy, Eötvös University Press, Budapest, 227–279, <https://doi.org/10.1180/EMU-notes.6.6>, 2004.
- Loh, E.: Optical vibrations in sheet silicates, *J. Phys. C Solid State*, 6, 1091–1104, 1973.
- McKeown, D. A., Bell, M. I., and Etz, E. S.: Raman spectra and vibrational analysis of the trioctahedral mica phlogopite, *Am. Mineral.*, 84, 970–976, 1999.
- Mihailova, B., Schlüter, J., and Harter-Uibopuu, K.: Inscribed gems: Material profiling beyond visible examination, in: *Exploring written artefacts: Objects, methods and concepts*, edited by: Quenzer, J. B., De Gruyter, Berlin, Boston, 229–244, <https://doi.org/10.1515/9783110753301-012>, 2021.
- Milke, R.: Geomaterials in the manuscript archive: The composition of writing sands and the regional distribution of writing-sand types in SW-Germany and northern Switzerland, 14th to 19th century, *Eur. J. Mineral.*, 24, 759–770, 2012.
- Momma, K. and Izumi, F.: VESTA: a three-dimensional visualization system for electronic and structural analysis, *J. Appl. Crystallogr.*, 41, 653–658, 2008.
- Prencipe, M., Mantovani, L., Tribaudino, M., Bersani, D., and Lotici, P. P.: The Raman spectrum of diopside: a comparison between *ab initio* calculated and experimentally measured frequencies, *Eur. J. Mineral.*, 24, 457–464, 2012.
- Redhammer, G. J., Beran, A., Schneider, J., Amthauer, G., and Lottermoser, W.: Spectroscopic and structural properties of synthetic micas on the annite-siderophyllite binary: Synthesis, crystal structure refinement, Mössbauer, and infrared spectroscopy, *Am. Mineral.*, 85, 449–465, 2000.
- Redhammer, G. J., Amthauer, G., Lottermoser, W., and Roth, G.: Quadrupole splitting distribution of Fe²⁺ in synthetic trioctahedral micas, *Hyperfine Interact.*, 141/142, 345–349, 2002.
- Redhammer, G. J., Amthauer, G., Lottermoser, W., Bernroider, M., Tippelt, G., and Roth, G.: X-ray diffraction and ⁵⁷Fe – Mössbauer spectroscopy of synthetic trioctahedral micas {K}[Me₃] < TSi₃ > O₁₀(OH)₂, Me = Ni²⁺, Mg²⁺, Co²⁺, Fe²⁺; T = Al³⁺, Fe³⁺, *Miner. Petrol.*, 85, 89–115, 2005.
- Rieder, M., Cavazzini, G., D’Yakonov, Y. S., Frank-Kamenetskii, V. A., Gottardi, G., Guggenheim, S., Koval, P. V., Müller, G., Neiva, A. M. R., Radoslovich, E. W., Robert, J.-L., Sassi, F. P., Takeda, H., Weiss, Z., and Wones, D. R.: Nomenclature of the micas, *Can. Mineral.*, 36, 1–10, 1998.
- Righter, K., Dyar, M. D., Delaney, J. S., Vennemann, T. W., Hervig, R. L., and King, P. L.: Correlations of octahedral cations with OH⁻, O²⁻, Cl⁻, and F⁻ in biotite from volcanic rocks and xenoliths, *Am. Mineral.*, 87, 142–153, 2002.
- Schingaro, E., Lacalamita, M., Scordari, F., and Mesto, E.: 3T-phlogopite from Kasenyi kamafugite (SW Uganda): EPMA, XPS, FTIR, and SCXRD study, *Am. Mineral.*, 98, 709–717, 2013.
- Scordari, F., Ventruti, G., Sabato, A., Bellatreccia, F., Della Ventura, G., and Pedrazzi, G.: Ti-rich phlogopite from Mt. Vulture (Potenza, Italy) investigated by a multianalytical approach: Substitutional mechanisms and orientation of the OH dipoles, *Eur. J. Mineral.*, 18, 379–391, 2006.
- Scordari, F., Schingaro, E., Ventruti, G., Lacalamita, M., and Ottolini, L.: Red micas from basal ignimbrites of Mt. Vulture

- (Italy): Interlayer content appraisal by a multi-methodic approach, *Phys. Chem. Miner.*, 35, 163–174, 2008.
- Scordari, F., Schingaro, E., Lacalamita, M., and Mesto, E.: Crystal chemistry of trioctahedral micas-2M₁ from Bunyaruguru kamafugite (southwest Uganda), *Am. Mineral.*, 97, 430–439, 2012.
- Scordari, F., Schingaro, E., Ventruti, G., Nicotra, E., Viccaro, M., and Mazziotti Tagliani, S.: Fluorophlogopite from Piano delle Concazze (Mt. Etna, Italy): Crystal chemistry and implications for the crystallization conditions, *Am. Mineral.*, 98, 1017–1025, 2013.
- Singha, M. and Singh, L.: Vibrational spectroscopic study of muscovite and biotite layered phyllosilicates, *Indian J. Pure Appl. Phys.*, 54, 116–122, 2016.
- Tlili, A., Smith, D. C., Beny, J.-M., and Boyer, H.: A Raman microprobe study of natural micas, *Mineral. Mag.*, 53, 165–179, 1989.
- Tutti, F. and Lazor, P.: Temperature-induced phase transition in phlogopite revealed by Raman spectroscopy, *J. Phys. Chem. Solids*, 69, 2535–2539, 2008.
- Uchida, E., Niikuma, D., and Watanabe, R.: Regional differences in the chemical composition of cuneiform clay tablets, *Archaeological Discovery*, 3, 179–207, 2015.
- Vedder, W.: Correlations between infrared spectrum and chemical composition of mica, *Am. Mineral.*, 49, 736–768, 1964.
- Velbel, M. A.: Formation of protective surface layers during silicate-mineral weathering under well-leached, oxidizing conditions, *Am. Mineral.*, 78, 405–414, 1993.
- Waeselmann, N., Schlüter, J., Malcherek, T., Della Ventura, G., Oberti, R., and Mihailova, B.: Nondestructive determination of the amphibole crystal-chemical formulae by Raman spectroscopy: One step closer, *J. Raman Spectrosc.*, 51, 1530–1548, 2020.
- Wang, A., Freeman, J. J., and Jolliff, B. L.: Understanding the Raman spectral features of phyllosilicates, *J. Raman Spectrosc.*, 46, 829–845, 2015.
- Wang, Y. Y., Gan, F. X., and Zhao, H. X.: Inclusions of black-green serpentine jade determined by Raman spectroscopy, *Vib. Spectrosc.*, 66, 19–23, 2013.
- Watenphul, A., Burgdorf, M., Schlüter, J., Horn, I., Malcherek, T., and Mihailova, B.: Exploring the potential of Raman spectroscopy for crystallochemical analyses of complex hydrous silicates: II. Tourmalines, *Am. Mineral.*, 101, 970–985, 2016a.
- Watenphul, A., Schlüter, J., Bosi, F., Skogby, H., Malcherek, T., and Mihailova, B.: Influence of the octahedral cationic-site occupancies on the framework vibrations of Li-free tourmalines, with implications for estimating temperature and oxygen fugacity in host rocks, *Am. Mineral.*, 101, 2554–2563, 2016b.
- Zazoff, P. (Ed.): *Die antiken Gemmen – Handbuch der Archäologie*, C.H. Beck'sche Verlagsbuchhandlung, Munich, Germany, ISBN 3406088961, 1983 (in German).